BeyondPlanck VI. Noise characterization and modelling

H. T. Ihle[11]⋆, M. Bersanelli[4, 9, 10], C. Franceschet[4, 10], E. Gjerløw[11], K. J. Andersen[11], R. Aurlien[11], R. Banerji[11], S. Bertocco[8], M. Brilenkov[11], M. Carbone[14], L. P. L. Colombo[4], H. K. Eriksen[11], J. R. Eskilt[11], M. K. Foss[11], U. Fuskeland[11], S. Galeotta[8], M. Galloway[11], S. Gerakakis[14], B. Hensley[2], D. Herman[11], M. Iacobellis[14], M. Ieronymaki[14], H. T. Ihle[11], J. B. Jewell[12], A. Karakci[11], E. Keihänen[3, 7], R. Keskitalo[1], G. Maggio[8], D. Maino[4, 9, 10], M. Maris[8], A. Mennella[4, 9, 10], S. Paradiso[4, 9], B. Partridge[6], M. Reinecke[13], M. San[11], A.-S. Suur-Uski[3, 7], T. L. Svalheim[11], D. Tavagnacco[8, 5], H. Thommesen[11], D. J. Watts[11], I. K. Wehus[11], and A. Zacchei[8]

[1] Computational Cosmology Center, Lawrence Berkeley National Laboratory, Berkeley, California, U.S.A.
[2] Department of Astrophysical Sciences, Princeton University, Princeton, NJ 08544, U.S.A.
[3] Department of Physics, Gustaf Hällströmin katu 2, University of Helsinki, Helsinki, Finland
[4] Dipartimento di Fisica, Università degli Studi di Milano, Via Celoria, 16, Milano, Italy
[5] Dipartimento di Fisica, Università degli Studi di Trieste, via A. Valerio 2, Trieste, Italy
[6] Haverford College Astronomy Department, 370 Lancaster Avenue, Haverford, Pennsylvania, U.S.A.
[7] Helsinki Institute of Physics, Gustaf Hällströmin katu 2, University of Helsinki, Helsinki, Finland
[8] INAF - Osservatorio Astronomico di Trieste, Via G.B. Tiepolo 11, Trieste, Italy
[9] INAF-IASF Milano, Via E. Bassini 15, Milano, Italy
[10] INFN, Sezione di Milano, Via Celoria 16, Milano, Italy
[11] Institute of Theoretical Astrophysics, University of Oslo, Blindern, Oslo, Norway
[12] Jet Propulsion Laboratory, California Institute of Technology, 4800 Oak Grove Drive, Pasadena, California, U.S.A.
[13] Max-Planck-Institut für Astrophysik, Karl-Schwarzschild-Str. 1, 85741 Garching, Germany
[14] Planetek Hellas, Leoforos Kifisias 44, Marousi 151 25, Greece

ABSTRACT

We present a Bayesian method for estimating instrumental noise parameters and propagating noise uncertainties within the global BeyondPlanck Gibbs sampling framework, and apply this to *Planck* LFI time-ordered data. Following previous literature, we adopt a simple $1/f$ model for the noise power spectral density (PSD), and implement an optimal Wiener-filter (or constrained realization) gap-filling procedure to account for masked data. We then use this procedure to both estimate the gapless correlated noise in the time-domain, $\boldsymbol{n}_{\mathrm{corr}}$, and to sample the noise PSD spectral parameters, $\xi^n = \{\sigma_0, f_{\mathrm{knee}}, \alpha\}$. In contrast to previous *Planck* analyses, we only assume piecewise stationary noise within each pointing period (PID), not throughout the full mission, but we adopt the LFI DPC results as priors on α and f_{knee}. On average, we find best-fit correlated noise parameters that are mostly consistent with previous results, with a few notable exceptions. However, a detailed inspection of the time-dependent results reveals many important findings. First and foremost, we find strong evidence for statistically significant temporal variations in all noise PSD parameters, many of which are directly correlated with satellite housekeeping data. Second, while the simple $1/f$ model appears to be an excellent fit for the LFI 70 GHz channel, there is evidence for additional correlated noise not described by a $1/f$ model in the 30 and 44 GHz channels, including within the primary science frequency range of 0.1–1 Hz. In general, most 30 and 44 GHz channels exhibit excess noise at the 2–3 σ level in each one hour pointing period. For some periods of time, we also find evidence of strong common mode noise fluctuations across the entire focal plane. Finally, we find a number of strong stripes when binning the 44 GHz correlated noise into a sky map, and we hypothesize that these may be associated with deficiencies in the gain model for this channel. Overall, we conclude that a simple $1/f$ profile is not adequate to fully characterize the *Planck* LFI noise, even when fitted hour-by-hour, and a more general model is required. These findings have important implications for large-scale CMB polarization reconstruction with the *Planck* LFI data, and understanding and mitigating these issues should be a high-priority task for future studies.

Key words. ISM: general – Cosmology: observations, polarization, cosmic microwave background, diffuse radiation – Galaxy: general

Contents

⋆ Corresponding author: H. T. Ihle; h.t.ihle@astro.uio.no

1. Introduction

One of the main algorithmic achievements made within the field of CMB analysis during the last few decades is accurate and nearly lossless data compression. Starting from data sets that typically comprise $O(10^8 - 10^{11})$ time-ordered measurements, we are now able to routinely produce sky maps that contain $O(10^3 - 10^7)$ pixels (e.g., Tegmark 1997; Ashdown et al. 2007). From these, we may constrain the angular CMB power spectrum, which spans $O(10^3)$ multipoles (e.g., Gorski 1994; Hivon et al. 2002; Wandelt et al. 2004). Finally, from these we may derive tight constraints on a small set of cosmological parameters (e.g., Bond et al. 2000; Lewis & Bridle 2002; Planck Collaboration V 2020; Planck Collaboration VI 2020), which typically is the ultimate goal of any CMB experiment.

Two fundamental assumptions underlying this radical compression process are that the instrumental noise may be modelled to a sufficient precision, and that the corresponding induced uncertainties may be propagated faithfully to higher-order data products. The starting point for this process is typically to assume that the noise is Gaussian and random in time, and does not correlate with the true sky signal at any given time. Under the Gaussian hypothesis, the net noise contribution therefore decreases as $1/\sqrt{N_{\mathrm{obs}}}$, where N_{obs} is the number of observations of the given pixel, while the signal contribution is independent of N_{obs}.

However, it is not sufficient to assume that the noise is simply Gaussian and random. One must also assume something about its statistical properties, both in terms of its correlation structure in time and its stationarity period. Regarding the correlation structure, the single most common assumption in the CMB literature is that the temporal noise power spectrum density (PSD) can be modelled as a sum of a so-called $1/f$ term and a white noise term (e.g., Bennett et al. 2013; Planck Collaboration II 2020; Planck Collaboration III 2020). The white noise term arises from intrinsic detector and amplifiers' thermal noise, and is substantially reduced by cooling the instrument to cryogenic temperatures, typically to ~20 K for coherent receivers (as in the case of *Planck* LFI) and to 0.1–0.3 K for bolometric detectors. Traditionally, the white noise of coherent radiometers is expressed in terms of system noise temperature, T_{sys}, per unit integration time (measured in K Hz$^{-1/2}$), while for bolometers it is expressed as noise equivalent power, NEP (W Hz$^{-1/2}$). The sources of the $1/f$ noise component include intrinsic instabilities in the detectors, amplifiers and readout electronics, as well as environmental effects, and, notably, atmospheric fluctuations for sub-orbital experiments. In the case of *Planck* LFI, the $1/f$ noise was dominated by gain and noise temperature fluctuations and thermal instabilities (Planck Collaboration II 2020), and was

minimized by introducing the 4 K reference loads and gain modulation factor to optimize the receiver balance; see, e.g., Planck Collaboration II (2014, 2016) and BeyondPlanck Collaboration (2020) for further details.

Regarding stationarity, the two most common assumptions are either that the statistical properties remain constant throughout the entire observation period (e.g., Planck Collaboration II 2020), or that it may at least be modelled as piece-wise stationary within for instance one hour of observations (e.g., QUIET Collaboration et al. 2011). Given such basic assumptions, the effect of the instrumental noise on higher-order data products has then traditionally been assessed, and propagated, either through the use of detailed end-to-end simulations (e.g., Planck Collaboration XII 2016) or in the form of explicit noise covariance matrices (e.g., Tegmark et al. 1997; Page et al. 2007; Planck Collaboration V 2020).

The importance of accurate noise modelling is intimately tied to the overall signal-to-noise ratio of the science target in question. For applications with very high signal-to-noise ratios, detailed noise modelling is essentially irrelevant, since other sources of systematic errors dominate the total error budget. One prominent example of this is the CMB temperature power spectrum as measured by *Planck* on large angular scales (Planck Collaboration IV 2020; Planck Collaboration V 2020). Its white noise contribution can be misestimated by orders of magnitude without making any difference in terms of cosmological parameters, because the full error budget is vastly dominated by cosmic variance.

The cases for which accurate noise modelling is critically important are those with signal-to-noise ratios of order unity. For these, noise misestimation may be the difference between obtaining a tantalizing, but ultimately unsatisfying, 2σ result, and claiming a ground-breaking and decisive 5σ discovery; or, the worst-case scenario, erroneously reporting a baseless positive detection.

This regime is precisely where the CMB field is expected to find itself in only a few years from now, as the next-generation CMB experiments (e.g., CMB-S4, *LiteBIRD*, *PICO*, Simons Observatory, and many others; Abazajian et al. 2019; Suzuki et al. 2018; Sugai et al. 2020; Hanany et al. 2019; Ade et al. 2019) are currently being planned, built and commissioned in the search for primordial gravitational waves imprinted in *B*-mode polarization. The predicted magnitude of this signal is expected to be at most a few tens of nanokelvins on angular scales larger than a degree, corresponding to a relative precision of $O(10^{-8})$, and extreme precision is required for a robust detection. It will therefore become critically important to take into account all sources of systematic uncertainties, and propagate these into the final results.

The BeyondPlanck project (BeyondPlanck Collaboration 2020) is an initiative that aims to meet this challenge by implementing the first global Bayesian CMB analysis pipeline that supports faithful end-to-end error propagation, from raw time-ordered data to final cosmological parameters. One fundamental aspect of this approach is a fully parametric data model that is fitted to the raw measurements through standard posterior sampling techniques, simultaneously constraining both instrumental and astrophysical parameters. Within this framework, the instrumental noise is just one among many different sources of uncertainty, all of which are treated on the same statistical basis. The sample-based approach introduced by BeyondPlanck therefore represents a novel and third way of propagating noise uncertainties (Keihänen et al. 2020; Suur-Uski et al. 2020), comple-

mentary to the existing simulation and covariance matrix based approaches used by traditional pipelines.

As a real-world demonstration of this novel framework, the BeyondPlanck collaboration has chosen the *Planck* LFI measurements (Planck Collaboration I 2020; Planck Collaboration II 2020) as its main scientific target (BeyondPlanck Collaboration 2020). These data represent an important and realistic testbed in terms of overall data volume and complexity, and they also have fairly well-understood properties after more than a decade of detailed scrutiny by the *Planck* team (see Planck Collaboration II 2014, 2016, 2020, and references therein). However, as reported in this paper, there are still a number of subtle unresolved and unexplored issues relating even to this important and well-studied data set that potentially may have an impact on higher-level science results. Furthermore, as demonstrated by the current analysis, the detailed low-level Bayesian modelling approach is ideally suited to identify, study and, eventually, mitigate these effects.

Thus, the present paper has two main goals. The first is to describe the general algorithmic framework implemented in the BeyondPlanck pipeline for modelling instrumental noise in CMB experiments. The second goal is then to apply these methods to the *Planck* LFI observations, and characterize the performance and systematic effects of the instrument as a function of time and detector.

The rest of the paper is organized as follows. First, in Sect. 2 we briefly review the BeyondPlanck analysis framework and data model, with a particular emphasis on noise modelling aspects. In Sect. 3, we present the individual sampling steps required for noise modelling, as well as some statistics that are useful for efficient data monitoring. In Sect. 4 we discuss various important degeneracies relevant for noise modelling, and how to minimize the impact of modelling errors. Next, in Sect. 5 we give a high-level overview of the various noise posterior distributions, their correlation properties, as well as detailed specifications for each detector. In Sect. 6 we discuss anomalies found in the data, and interpret these in terms of the instrument and the thermal environment. Finally, we summarize in Sect. 7.

2. The BeyondPlanck data model and framework

The BeyondPlanck project is an attempt to build up an end-to-end data analysis pipeline for CMB experiments going all the way from raw time-ordered data to cosmological parameters in a consistent Bayesian framework. This allows us to characterize degeneracies between instrumental and astrophysical parameters in a statistically well-defined framework, from low-level instrumental quantities such as gain (Gjerløw et al. 2020), bandpasses (Svalheim et al. 2020a), far sidelobes (Galloway et al. 2020b), and correlated noise via Galactic parameters such as the synchrotron amplitude or spectral index (Andersen et al. 2020; Svalheim et al. 2020b), to the angular CMB power spectrum and cosmological parameters (Colombo et al. 2020; Paradiso et al. 2020).

The LFI dataset consists of three bands, at frequencies of roughly 30, 44, and 70 GHz. These bands have two, three, and six radiometer pairs each, respectively, which for historical reasons are numbered from 18 to 28. The two radiometers in each pair are labeled by M and S (Planck Collaboration II 2014). In BeyondPlanck, the raw uncalibrated data, d, produced by each

of these radiometers is modelled in time-domain as follows,

$$d_{j,t} = g_{j,t} \mathsf{P}_{tp,j} \left[\mathsf{B}^{\mathrm{symm}}_{pp',j} \sum_c \mathsf{M}_{cj}(\beta_{p'}, \Delta^j_{\mathrm{bp}}) a^c_{p'} + \mathsf{B}^{\mathrm{asymm}}_{pp',j} \left(s^{\mathrm{orb}}_{j,t} + s^{\mathrm{fsl}}_{j,t} \right) \right] + \\ + n^{\mathrm{corr}}_{j,t} + n^{\mathrm{w}}_{j,t}.$$

(1)

Here the subscript t denotes a sample index in time domain; j denotes radiometer; p denotes the pixel number; c denotes signal component; g denotes the gain; P denotes the pointing matrix; $\mathsf{B}^{\mathrm{symm}}$ and $\mathsf{B}^{\mathrm{asymm}}$ denote the symmetric and asymmetric beam matrices, respectively; a are the astrophysical signal amplitudes; β are the corresponding spectral parameters; Δ_{bp} are the bandpass corrections; M_{cj} is the bandpass-dependent component mixing matrix; s^{orb} is the orbital dipole; s^{fsl} are the far sidelobe corrections; n^{corr} is the correlated noise; and n^{w} is the white noise. For more details on each of these parameters see BeyondPlanck Collaboration (2020) and the other companion papers.

The goal of the Bayesian approach is now to sample from the joint posterior distribution ,

$$P(g, n_{\mathrm{corr}}, \xi_n, \Delta_{\mathrm{bp}}, a, \beta, C_\ell \mid d). \tag{2}$$

This is a large and complicated distribution, with many degeneracies. However, using Gibbs sampling we can divide the sampling process into a set of managable steps. Gibbs sampling is a simple algorithm in which samples from a joint multi-dimensional distribution are generated by iterating through all corresponding conditional distributions. Using this method, the BeyondPlanck sampling scheme may be summarized as follows (BeyondPlanck Collaboration 2020),

$$g \leftarrow P(g \quad \mid d, \qquad \xi_n, \Delta_{\mathrm{bp}}, a, \beta, C_\ell) \tag{3}$$

$$n_{\mathrm{corr}} \leftarrow P(n_{\mathrm{corr}} \mid d, g, \qquad \xi_n, \Delta_{\mathrm{bp}}, a, \beta, C_\ell) \tag{4}$$

$$\xi_n \leftarrow P(\xi_n \quad \mid d, g, n_{\mathrm{corr}}, \qquad \Delta_{\mathrm{bp}}, a, \beta, C_\ell) \tag{5}$$

$$\Delta_{\mathrm{bp}} \leftarrow P(\Delta_{\mathrm{bp}} \mid d, g, n_{\mathrm{corr}}, \xi_n, \qquad a, \beta, C_\ell) \tag{6}$$

$$\beta \leftarrow P(\beta \quad \mid d, g, n_{\mathrm{corr}}, \xi_n, \Delta_{\mathrm{bp}}, \qquad C_\ell) \tag{7}$$

$$a \leftarrow P(a \quad \mid d, g, n_{\mathrm{corr}}, \xi_n, \Delta_{\mathrm{bp}}, \quad \beta, C_\ell) \tag{8}$$

$$C_\ell \leftarrow P(C_\ell \quad \mid d, g, n_{\mathrm{corr}}, \xi_n, \Delta_{\mathrm{bp}}, a, \beta \quad). \tag{9}$$

Here, $\leftarrow$ indicates sampling from the distribution on the right-hand side.

Note that for some of these steps we are not following the strict Gibbs approach of conditioning on all but one variable. Most notably for us, this is the case for the gain sampling step in Eq. (3), where we do not condition on n_{corr}. In effect, we instead sample the gain and correlated noise jointly by exploiting the definition of a conditional distribution,

$$P(g, n_{\mathrm{corr}} \mid d, \cdots) = P(g \mid d, \cdots) P(n_{\mathrm{corr}} \mid d, g, \cdots). \tag{10}$$

This equation implies that a joint sample $\{g, n_{\mathrm{corr}}\}$ may be produced by first sampling the gain from the marginal distribution with respect to n_{corr}, and then sampling n_{corr} from the usual conditional distribution with respect to g. The advantage of this joint sampling procedure is a much shorter Markov correlation length as compared to standard Gibbs sampling, as discussed by Gjerløw et al. (2020).

A convenient property of Gibbs sampling is its modular nature, as the various parameters are sampled independently within each conditional distribution, but joint dependencies are still explored through the iterative scheme. In this paper, we are therefore only concerned with two of the above steps, namely Eqs. (4)

and (5). For details on the complete Gibbs chain and the other sampling steps, see BeyondPlanck Collaboration (2020) and the companion papers.

The LFI time-ordered data are divided into roughly 45 000 pointing periods, denoted PIDs (pointing ID). Most PIDs have a duration of 30–60 minutes. When sampling the correlated noise and the corresponding PSD parameters, we assume that the noise is stationary within each PID, but independent between PIDs. The gain is also assumed to be constant within each PID; however, this is not fit independently for each PID, but rather sampled smoothly on longer timescales (Gjerløw et al. 2020).

Following previous literature (Planck Collaboration II 2014; Tauber et al. 2019; Planck Collaboration II 2020), we assume that the LFI noise PSD can be described by a so-called $1/f$ model,

$$P(f) = \sigma_0^2 \left[1 + \left(\frac{f}{f_{\text{knee}}} \right)^{\alpha} \right]. \tag{11}$$

Here f denotes a temporal frequency; σ_0 quantifies the white noise level of the time-ordered data[1]; α is the slope (typically negative) of the correlated noise spectrum; and the knee frequency, f_{knee}, denotes the (temporal) frequency at which the variance of the correlated noise is equal to the white noise variance. The three PSD parameters are collectively denoted $\xi_n = \{\sigma_0, f_{\text{knee}}, \alpha\}$. Note, however, that there is nothing unique or fundamental about the $1/f$ noise model, and a real-world instrument may exhibit a more complicated noise structure than this. Determining whether Eq. (11) represents a statistically acceptable model for the LFI noise is an important goal of the current paper.

3. Methods

As outlined above, noise estimation in the Bayesian BEYOND-PLANCK framework amounts essentially to being able to sample from two conditional distributions, namely $P(\boldsymbol{n}_{\text{corr}} \mid \boldsymbol{d}, \omega \setminus \boldsymbol{n}_{\text{corr}})$ and $P(\xi_n \mid \boldsymbol{d}, \omega \setminus \xi_n)$. The first presentation of Bayesian noise estimation for time-ordered CMB data that was applicable to the current problem was presented by Wehus et al. (2012), and the main novel feature presented in the current paper is simply the integration of these methods into the larger end-to-end analysis framework outlined above. In addition, the current analysis also employs important numerical improvements as introduced by Keihänen et al. (2020), in which optimal mapmaking is rephrased into an efficient Bayesian language.

The starting point for both conditional distributions is the following parametric data model,

$$\boldsymbol{d} = g\boldsymbol{s}^{\text{tot}} + \boldsymbol{n}^{\text{corr}} + \boldsymbol{n}^{\text{wn}}, \tag{12}$$

where $\boldsymbol{d}$ denotes the raw time ordered data (TOD) organized into a column vector; g is the gain; $\boldsymbol{s}^{\text{tot}}$ describes the total sky signal, comprising both CMB and foregrounds, projected into time-domain; $\boldsymbol{n}^{\text{corr}}$ represents the correlated noise in time domain; and $\boldsymbol{n}^{\text{wn}}$ is white noise. The two noise terms are both assumed to be Gaussian distributed with covariance matrices $\mathsf{N}_{\text{corr}} \equiv \langle \boldsymbol{n}_{\text{corr}} \boldsymbol{n}_{\text{corr}}^T \rangle$ and $\mathsf{N}_{\text{wn}} \equiv \langle \boldsymbol{n}_{\text{wn}} \boldsymbol{n}_{\text{wn}}^T \rangle$, respectively. The complete noise PSD is then given by $P(f) = \mathsf{N}_{\text{wn}} + \mathsf{N}_{\text{corr}} = \sigma_0^2 + \sigma_0^2 \left(\frac{f}{f_{\text{knee}}} \right)^{\alpha}$.

---

[1] σ_0 has different units if we are talking about the uncalibrated data, σ_0 [V], calibrated data, σ_0 [K] $\equiv \sigma_0$ [V] $/g$, or the white noise PSD, σ_0^2 [K^2 Hz^{-1}] $\equiv (\sigma_0$ [K]$)^2 \frac{2}{R_{\text{samp}}}$, where R_{samp} is the sample rate (in Hz) of the time ordered data. Where this distinction is important, we include the units explicitly.

3.1. Sampling correlated noise, $P(\boldsymbol{n}^{\text{corr}} \mid \boldsymbol{d}, \xi^n, \boldsymbol{s}_{\text{tot}}, g)$

Our first goal is to derive an appropriate sampling prescription for the time-domain correlated noise conditional distribution, $P(\boldsymbol{n}^{\text{corr}} \mid \boldsymbol{d}, \xi^n, \boldsymbol{s}_{\text{tot}}, g)$. To this end, we start by defining the signal-subtracted data, $\boldsymbol{d}'$, directly exploiting the fact that g and s^{tot} are currently conditioned upon,[2]

$$\boldsymbol{d}' \equiv \boldsymbol{d} - g\boldsymbol{s}^{\text{tot}} = \boldsymbol{n}^{\text{corr}} + \boldsymbol{n}^{\text{wn}}. \tag{13}$$

Since both $\boldsymbol{n}^{\text{corr}}$ and $\boldsymbol{n}^{\text{wn}}$ are assumed Gaussian with known covariance matrices, the appropriate sampling equation for $\boldsymbol{n}^{\text{corr}}$ is also that of a multivariate Gaussian distribution, which is standard textbook material; for a brief review, see Appendix A in BeyondPlanck Collaboration (2020). In particular, the maximum likelihood (ML) solution for n_t^{corr} is given by the so-called Wiener-filter equation,

$$\left(\mathsf{N}_{\text{corr}}^{-1} + \mathsf{N}_{\text{wn}}^{-1} \right) \boldsymbol{n}^{\text{corr}} = \mathsf{N}_{\text{wn}}^{-1} \boldsymbol{d}', \tag{14}$$

while a random sample of $\boldsymbol{n}^{\text{corr}}$ may be found by solving the following equation,

$$\left(\mathsf{N}_{\text{corr}}^{-1} + \mathsf{N}_{\text{wn}}^{-1} \right) \boldsymbol{n}^{\text{corr}} = \mathsf{N}_{\text{wn}}^{-1} \boldsymbol{d}' + \mathsf{N}_{\text{wn}}^{-1/2} \boldsymbol{\eta}_1 + \mathsf{N}_{\text{corr}}^{-1/2} \boldsymbol{\eta}_2, \tag{15}$$

where $\boldsymbol{\eta}_1$ and $\boldsymbol{\eta}_2$ are two independent vectors of random variates drawn from a standard Gaussian distribution, $\boldsymbol{\eta}_{1,2} \sim \mathcal{N}(\mu = 0, \sigma^2 = 1)$.

3.1.1. Ideal data

Assuming for the moment that both N_{corr} and N_{wn} are diagonal in Fourier space, we note that Eq. (15) may be solved in a closed form in Fourier space,

$$n_f^{\text{corr}} = \frac{d_f' + C \left(\mathsf{N}_{\text{wn}}^{1/2}(f) w_1 + \mathsf{N}_{\text{wn}}(f) \mathsf{N}_{\text{corr}}^{-1/2}(f) w_2 \right)}{1 + \mathsf{N}_{\text{wn}}(f)/\mathsf{N}_{\text{corr}}(f)}, \tag{16}$$

for any non-negative frequency f, where the correlated noise TOD has been decomposed as $n_f^{\text{corr}} = \sum_t n_t^{\text{corr}} e^{-2\pi i f t}$. For completeness, C is a constant factor that depends on the Fourier convention of the numerical library of choice,[3] and $w_{1,2}$ are two independent random complex samples from a Gaussian distribution,

$$w_{1,2} \equiv \frac{\eta_R + i\eta_I}{\sqrt{2}}, \tag{17}$$

where $\eta_{R,I} \sim \mathcal{N}(\mu = 0, \sigma^2 = 1)$.

Figure 1 shows three independent realizations of $\boldsymbol{n}^{\text{corr}}$ that all correspond to the same signal-subtracted *Planck* 30 GHz TOD segment. Each correlated noise sample is essentially a Wiener-filtered version of the original data, and traces as such the slow variations in the data, with minor variations corresponding the two random fluctuation terms in Eq. (16), as allowed by the white noise level present in the data. We can also see that there are gaps in the data, which we will need to deal with.

---

[2] When a parameter appears on the right-hand side of a conditioning bar in a probability distribution, it is assumed known to infinite precision. It is therefore for the moment a constant quantity, and not associated with any stochastic degrees of freedom or uncertainties.

[3] We use the FFTW library, in which case $C = \sqrt{n_{\text{samples}}}$, where n_{samples} is the number of time samples.
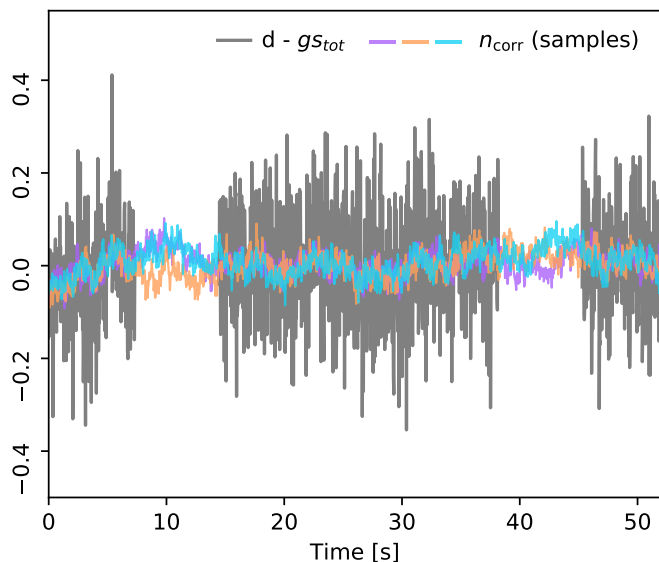
Fig. 1. Illustration of three constrained correlated noise realizations (colored curves) drawn from $P(n^{corr} \mid d, \xi^n, s_{tot}, g)$ for the *Planck* 30 GHz data (grey curve). Regions for which parts of the data have been masked, either due to a processing mask or flagged data, are marked as white gaps.

Fig. 2. Illustration of the limitation of the linear gap-filling procedure for simulated data with extreme noise properties and large gaps. In general, the linear gap-filling procedure tends to underestimate the fluctuations in n^{corr} on long timescales.

3.1.2. Handling masking through a conjugate gradient solver

When writing down an explicit solution of Eq. (15) in Eq. (16), we assumed that both N_{corr} and N_{wn} were diagonal in Fourier space. However, as illustrated in Fig. 1, real observations have gaps, either because of missing or flagged data. The most typical example of missing data is the application of a processing mask that removes all samples with too strong foreground contamination, either from Galactic diffuse sources or from extragalactic point sources.

We can represent these gaps in our statistical model by setting the white noise level for masked samples to infinity. This ensures that Eqs. (14) and (15) are still well defined, albeit somewhat harder to solve. The new difficulty lies in the fact that while N_{wn} is still diagonal in the time domain, it is no longer diagonal in the Fourier domain. This problem may be addressed in two ways. Specifically, we can either solve Eqs. (14) and (15) directly, using an iterative method such as the conjugate gradient (CG) method (Wehus et al. 2012; Keihänen et al. 2020), or we can fill any gap in d' with a simpler interpolation scheme, for instance a polynomial plus white noise, and then use Eq. (16) directly. Clearly, the former method is mathematically superior, as it results in a statistically exact result. However, the CG method is in general not guaranteed to converge due to numerical round-off errors, and since the current algorithm is to be applied millions of times in a Monte Carlo environment, the second approach is useful as a fallback solution for the few cases for which the exact CG approach fails.

As shown by Keihänen et al. (2020), Eq. (15) may be recast into a compressed form using the Sherman-Morrison-Woodbury formula, effectively separating the masked from the unmasked degrees of freedom, and the latter may then be handled with the direct formula in Eq. (16). This approach, in addition to having a lower computational cost per CG iteration, also needs fewer iterations to converge compared to the untransformed equation.
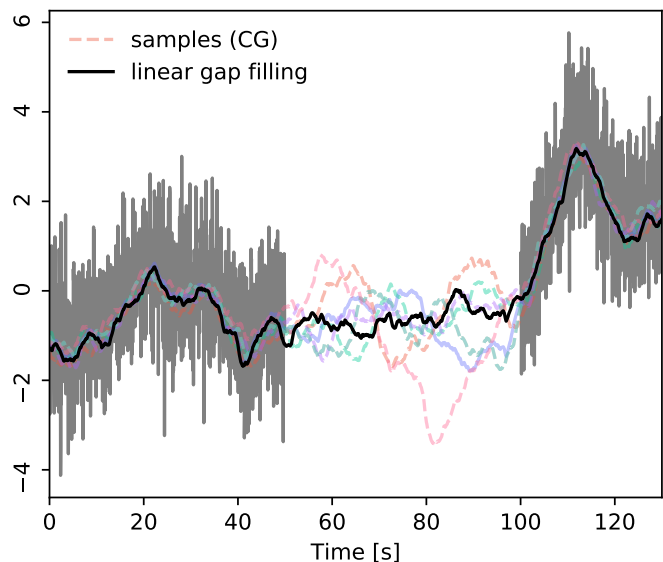
We adopt this approach without modifications for the main BeyondPlanck pipeline.

Returning to Fig. 1, we note that the correlated noise samples have significant larger variance within the gaps than in the data-dominated regime. As a result, one should expect to see a slightly higher conditional χ^2 inside the processing mask in a full analysis than outside, since n^{corr} will necessarily trace the real data less accurately in that range. This is in fact seen in the main BeyondPlanck analysis, as reported by BeyondPlanck Collaboration (2020) and Suur-Uski et al. (2020). However, when marginalizing over all allowed correlated noise realizations, the final uncertainties will be statistically appropriate, due to the fluctuation terms in Eq. (15).

3.1.3. Gap-filling by polynomial interpolation

As mentioned above, the CG algorithm does not always converge, and for Monte Carlo applications that will run millions of times without human supervision, it is useful to establish a robust fallback solution. For this purpose, we adopt the basic approach of simply interpolating between the values on each side of a gap. Specifically, we compute the average of the non-masked points among the 20 points on each side of the gap, and interpolate linearly between these two values. In addition, we add a white noise component to d', based on N^{wn}, to each masked sample.

An important limitation of the linear gap-filling procedure is associated with estimation of the noise PSD parameters, ξ^n. As described in Sect. 3.2, these parameters are estimated directly from n^{corr} by Gibbs sampling. A statistically suboptimal sample of n^{corr} may therefore also bias ξ^n, which in turn may skew n^{corr} even further. If the gaps are short, then this bias is usually negligible, but for large gaps it can be problematic. This situation is illustrated in Fig. 2, which compares the linear gap filling procedure with the exact CG approach. In general, the linear method tends to underestimate the fluctuations on large timescales within the gap.

Because of the close relative alignment of the *Planck* scanning strategy with the Galactic plane that takes place every six months (Planck Collaboration I 2011), some pointing periods happen to have larger gaps than others. For these, two long masked regions occur every minute, when the telescope points toward the Galactic plane. Any systematic bias introduced by the gap-filling procedure itself will then not be randomly distributed in the TOD, but rather systematically contribute to the same modes, with a specific period equal to the satellite spin rate. For these, the statistical precision of the CG algorithm is particularly important to avoid biased noise parameters.

Overall, the linear gap filling procedure should only be used when strictly necessary. In practice, we use it only when the CG solver fails to converge within 30 iterations, which happens in less than 0.03 % of all cases.

Another simpler and more accurate gap filling procedure is suggested by Keihänen et al. (2020): We may simply fill the gaps in d' with the previous sample of the correlated noise, and then add white noise fluctuations. This corresponds to Gibbs sampling over the white noise as a stochasic parameter, which is statistically fully valid. However, this approach requires us to store the correlated noise TOD in memory between consecutive Gibbs iterations. Since memory use is already at its limit (Galloway et al. 2020a), this method is not used for the main BEYONDPLANCK analysis. However, for systems with more available RAM, this method is certainly preferable over simple linear interpolation.

3.2. Sampling noise PSD parameters, $P(\xi^n \mid n^{\mathrm{corr}})$

The second noise-related conditional distribution in the BEYOND-PLANCK Gibbs chain is $P(\xi^n \mid n^{\mathrm{corr}})$, which describes the noise PSD. As discussed in Sect. 2, in this paper we model this function in terms of a $1/f$ spectrum as defined by Eq. (11). We emphasize, however, that any functional form for $P(f)$ may be fitted using the methods described below. Figure 3 illustrates the PSD of the different components, and our task is now to sample each of the noise PSD parameters $\xi^n = \{\sigma_0, f_{\mathrm{knee}}, \alpha\}$, corresponding to the dashed blue line in this figure.

3.2.1. Sampling the white noise level, σ_0

We start with the white noise level, which by far is the most important noise PSD parameter in the system. We first note from Eq. (11) that if α is close to zero, the correlated and white noise terms are perfectly degenerate. Even for $\alpha \approx -1$ there is a significant degeneracy between the two components for a finite-length TOD.

Of course, for other parameters in the full Gibbs chain, only the combined $P(f)$ function is relevant, and not each component separately. At the same time, and as described by BeyondPlanck Collaboration (2020), marginalization over the two terms within other sampling steps happens using two fundamentally different methods: While white noise marginalization is performed analytically through a diagonal covariance matrix, marginalization over correlated noise is done by Monte Carlo sampling of n^{corr}. It is therefore algorithmically advantageous to make sure that the white noise term accounts for as much as possible of the full noise variance, as this will lead to an overall shorter Markov chain correlation length.

For this reason, we employ a commonly used trick in radio astronomy for estimating the white noise level, and define this to be

$$\sigma_0^2 \equiv \frac{\mathrm{Var}(r_{i+1} - r_i)}{2}, \tag{18}$$
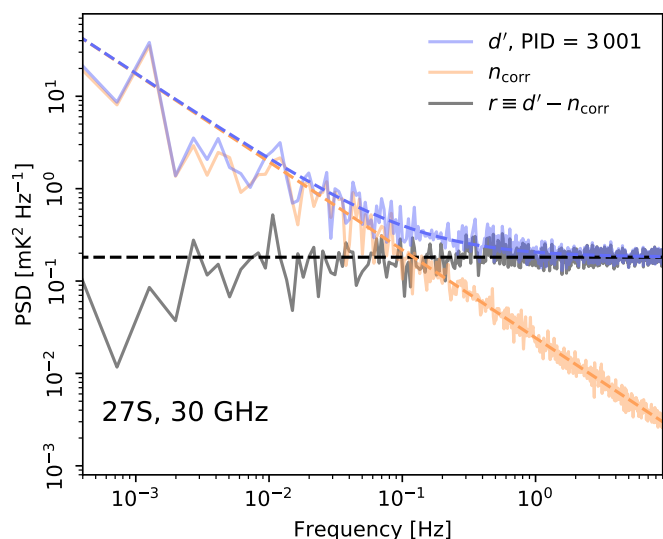
Fig. 3. Comparison of temporal PSDs for different components. The blue curve shows the PSD of the signal-subtracted data; the orange curve shows the fitted correlated noise PSD; and the gray line shows the PSD of the residual TOD. The dashed curves correspond to the best fit $1/f$-noise model, with (blue) and without (orange) white noise.

where $r \equiv d' - n^{\mathrm{corr}}$. By differencing consecutive samples, any residual temporal correlations are effectively eliminated, and will therefore not bias the determination of σ_0.

This method is equivalent to fixing the white noise level to the highest frequencies in Fig. 3. Formally speaking, this means that σ_0 should not be considered a free parameter within the Gibbs chain, but rather a derived quantity fixed by the data, d, the gain, g, the signal model, s^{tot}, and the correlated noise, n^{corr}. However, this distinction does not carry any particular statistical significance with respect to other parameters, and we will in the following therefore discuss σ_0 on the same footing as any of the other noise parameters.

3.2.2. Sampling correlated noise parameters, f_{knee} and α

With σ_0^2 fixed by Eq. (18), the other noise parameters, f_{knee} and α, are sampled from their exact conditional distributions. Since we assume that also the correlated noise component is Gaussian distributed, the appropriate functional form is that of a multivariate Gaussian,

$$P(f_{\mathrm{knee}}, \alpha \mid \sigma_0, n^{\mathrm{corr}}) \propto \frac{e^{-\frac{1}{2}(n^{\mathrm{corr}})^T N_{\mathrm{corr}}^{-1} n^{\mathrm{corr}}}}{\sqrt{|N_{\mathrm{corr}}|}} P(f_{\mathrm{knee}}, \alpha), \tag{19}$$

where $N_{\mathrm{corr}} = N_{\mathrm{corr}}(f_{\mathrm{knee}}, \alpha)$, and $P(f_{\mathrm{knee}}, \alpha)$ is an optional prior. This may be efficiently evaluated in Fourier space as

$$-\ln P = \sum_{f=f_{\mathrm{min}}}^{f_{\mathrm{max}}} \left[\frac{|n_f^{\mathrm{corr}}|^2}{N_{\mathrm{corr}}(f)} + \ln N_{\mathrm{corr}}(f) \right] - \ln P(f_{\mathrm{knee}}, \alpha), \tag{20}$$

where $N_{\mathrm{corr}}(f) = \sigma_0^2 \left(\frac{f}{f_{\mathrm{knee}}} \right)^{\alpha}$.

To explore this joint distribution, we iteratively Gibbs sample over f_{knee} and α, using an inversion sampler for each of the two conditional distributions, $P(f_{\mathrm{knee}} \mid \alpha, \sigma_0, n^{\mathrm{corr}})$ and $P(\alpha \mid f_{\mathrm{knee}}, \sigma_0, n^{\mathrm{corr}})$; see Appendix A in BeyondPlanck Collaboration (2020) for details regarding the inversion sampler.
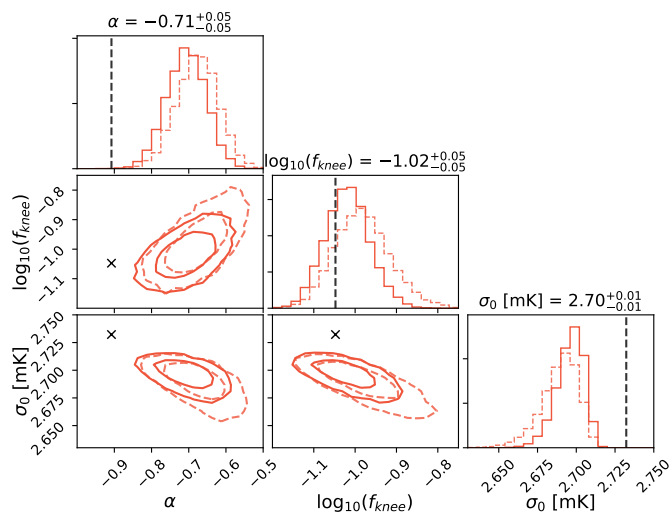
Fig. 4. Distribution of noise parameters for PID 10101 of radiometer 24S, one of the 44 GHz channels, for fixed s_{tot} and g. Dashed red lines correspond to results obtained without an active prior, while the solid line corresponds to results after including the active priors on f_{knee} and α from Eqs. (21) and (22). Black crosses indicate the best fit values derived by the DPC pipeline for this radiometer.

If we naively apply our statistical model, all frequencies should in principle be included in the sum in Eq. (20). At the same time, we note that frequencies well above f_{knee} ideally should carry very little statistical weight, since the correlated noise variance then by definition is smaller than the white noise variance. This means that the sampled $\boldsymbol{n}^{\mathrm{corr}}$ is almost completely determined by the prior (i.e., the previous values of $\sigma_0, f_{\mathrm{knee}}, \alpha$), at these high frequencies. The sum in Eq. (20), on the other hand, is completely dominated by those high frequencies. The result of this is an excessively long Markov chain correlation length when including all frequencies in Eq. (20); the inferred values of α and f_{knee} will always be extremely close to the previous values.

One way to avoid these long correlation lengths would be not to condition on $\boldsymbol{n}^{\mathrm{corr}}$ at all, but rather use the likelihood for $\boldsymbol{d}'$ to sample α and f_{knee} (and sample $\boldsymbol{n}^{\mathrm{corr}}$ afterwards). This is equivalent to sampling ξ^n from the marginal distribution with respect to $\boldsymbol{n}^{\mathrm{corr}}$, and fully analogous to how the degeneracy between g and $\boldsymbol{n}^{\mathrm{corr}}$ is broken through joint sampling. However, for real world data, residual signal or systematics may leak into $\boldsymbol{d}'$, in particular at frequencies around and above the satellite scanning frequency. While some of these systematics may also leak into $\boldsymbol{n}^{\mathrm{corr}}$, in general $\boldsymbol{n}^{\mathrm{corr}}$ is cleaner, especially at frequencies below f_{knee}, where $\boldsymbol{n}^{\mathrm{corr}}$ is dominated by the random sampling terms.

A useful solution that both makes the correlated noise parameters robust against modelling errors and results in a short Markov chain correlation length is therefore to condition on $\boldsymbol{n}^{\mathrm{corr}}$ above some pre-specified frequency. In practice, we therefore choose to only include frequencies below $f_{\mathrm{max}} = 2f_{\mathrm{knee}}^{\mathrm{DPC}}$ when evaluating Eq. (20), where $f_{\mathrm{knee}}^{\mathrm{DPC}}$ is the knee frequency determined by the *Planck* LFI Data Processing Center (DPC, Planck Collaboration II 2020). That is, we only use the part of $\boldsymbol{n}^{\mathrm{corr}}$ where we are able to measure the $1/f$ slope with an appreciable signal to noise ratio. For the lower frequency cutoff in Eq. (20), we adopt $f_{\mathrm{min}} > 0$, and only exclude the overall mean per PID.

3.2.3. Priors on α and f_{knee}

As described by Planck Collaboration II (2020), the official *Planck* LFI DPC analyses assume the noise PSD to be stationary throughout the mission. Here we allow these parameters to vary from PID to PID, in order to accommodate possible changes in the thermal environment of the satellite. However, since the duration of a single PID is typically one hour or shorter, there is only a limited number of large-scale frequencies available to estimate the correlated noise parameters, and this may in some cases lead to significant degeneracies between α and f_{knee}. In particular, if f_{knee} is low (which of course is the ideal case), α is essentially unconstrained. To avoid pathological cases, it is therefore useful to impose priors on each of these parameters, under the assumption that the system should be relatively stable as a function of time.

Specifically, we adopt a log-normal prior for f_{knee},

$$-\ln P(f_{\mathrm{knee}}) = \frac{1}{2}\left(\frac{\log_{10} f_{\mathrm{knee}} - \log_{10} f_{\mathrm{knee}}^{\mathrm{DPC}}}{\sigma_{f_{\mathrm{knee}}}}\right)^2 + \ln f_{\mathrm{knee}}, \qquad (21)$$

where $f_{\mathrm{knee}}^{\mathrm{DPC}}$ is the DPC result for a given radiometer (Planck Collaboration II 2020) and $\sigma_{f_{\mathrm{knee}}} = 0.1$. For α, we adopt a Gaussian prior of the form

$$-\ln P(\alpha) = \frac{1}{2}\left(\frac{\alpha - \alpha^{\mathrm{DPC}}}{\sigma_\alpha}\right)^2, \qquad (22)$$

where α^{DPC} again is the DPC result for the given radiometer and $\sigma_\alpha = 0.2$. Figure 4 shows a comparison of the posterior distributions with (solid lines) and without (dashed lines) active priors for a typical example.

The prior widths have been chosen to be sufficiently loose that the overall impact of the priors is moderate for most cases. The priors are in practice only used to exclude pathological cases. Technically speaking, we also impose absolute upper and lower limits for each parameter, as this is needed for gridding the conditional distribution within the inversion sampler. However, the limits are chosen to be sufficiently wide so that they have no significant impact on final results.

4. Mitigation of modelling errors and degeneracies

When applying the methods described above to real-world data as part of a larger Gibbs chain, several other degeneracies and artifacts may emerge beyond those discussed above. In this section, we discuss some of the main challenges for the current setup, and we also describe solutions to break or mitigate these issues.

4.1. Signal modelling errors and processing masks

First, we note that the correlated noise component is by nature entirely instrument specific, and depends directly on the thermal stability of the detectors. It is therefore difficult to impose any strong spatial priors on $\boldsymbol{n}^{\mathrm{corr}}$, beyond the loose PSD priors described above, and these provide only very weak constraints in map-domain. The correlated noise is from first principles the least known parameter in the entire model, and its allowed parameter space is able to describe a wide range of different TOD combinations, without inducing a significant likelihood penalty relative to the $1/f$ model. As a result, a wide range of systematic

errors or model mismatches may be described quite accurately by modifying $\boldsymbol{n}^{\text{corr}}$, rather than ending up in the residual,

$$\boldsymbol{r} \equiv \boldsymbol{d} - \boldsymbol{n}^{\text{corr}} - g\boldsymbol{s}_{\text{tot}}. \tag{23}$$

Colloquially speaking, the correlated noise component may in many respects be considered the "trash can" of CMB time-ordered analysis, capturing anything that does not fit elsewhere in the model. This is both a strength and a weakness. On the one hand, the flexibility of $\boldsymbol{n}^{\text{corr}}$ protects against modelling errors for other (and far more important) parameters in the model, including the CMB parameters. On the other hand, in many cases it is preferable that modelling errors show up as χ^2 excesses, so that they can be identified and mitigated, rather than leaking into the correlated noise. To check for different types of modelling errors, it is therefore extremely useful to inspect both χ^2's and binned sky maps of $\boldsymbol{r}_\nu$ and $\boldsymbol{n}^{\text{corr}}$ for artifacts. For an explicit example of this, see the discussion of data selection for BeyondPlanck in Suur-Uski et al. (2020), where these statistics are used as efficient tools to identify bad observations.

In general, the most problematic regions of the sky are those with bright foregrounds, either in the form of diffuse Galactic emission or strong compact sources. If residuals from such foregrounds are present in the signal-subtracted data, $\boldsymbol{d}'$, while estimating the correlated noise TOD, the correlated noise Wiener filter in Eq. (15) will attempt to fit these in $\boldsymbol{n}^{\text{corr}}$, and this typically results in stripes along the scanning path with a correlation length defined by the ratio between f_{knee} and the scanning frequency.

To suppress such artifacts, we impose a processing mask for each frequency, as discussed in Sect. 3.1. In the current analysis, we define these masks as follows:

1. We bin the time-domain residual in Eq. (23) into an *IQU* pixelized sky map for each frequency (as defined by Eq. (77) in BeyondPlanck Collaboration 2020), and smooth this map to an angular resolution of 10° FWHM.
2. We take the absolute value of the smoothed map, and then smooth again with a 30′ beam to account for pixels which the raw residual map changes sign.
3. We then compute the maximum absolute value for each pixel over each of the three Stokes parameters. The resulting maps are shown in Fig. 5 for each of the three *Planck* LFI frequencies.
4. These maps are then thresholded at values well above the noise level, and these tresholded maps form the main input to the processing masks.
5. To remove particularly bright compact objects that may not be picked up by the smooth residual maps described above, we additionally remove all pixels with high free-free and/or AME levels, as estimated in an earlier analysis.

The final processing masks are shown in Fig. 6, and allow 73, 81, and 77 % of the sky to be included while fitting correlated noise at 30, 44, and 70 GHz, respectively.

4.2. Degeneracies with the gain

The brightest component of the entire BeyondPlanck signal model is the Solar CMB dipole, which has an amplitude of 3 mK. This component plays a critical role in terms of gain estimation (Gjerløw et al. 2020), and serves as the main tool to determine relative calibration differences between detectors. Both the gain and CMB dipole parameters are of course intrinsically unknown quantities, and must be fitted jointly. Any error in the determination of these will therefore necessarily result in a nonzero
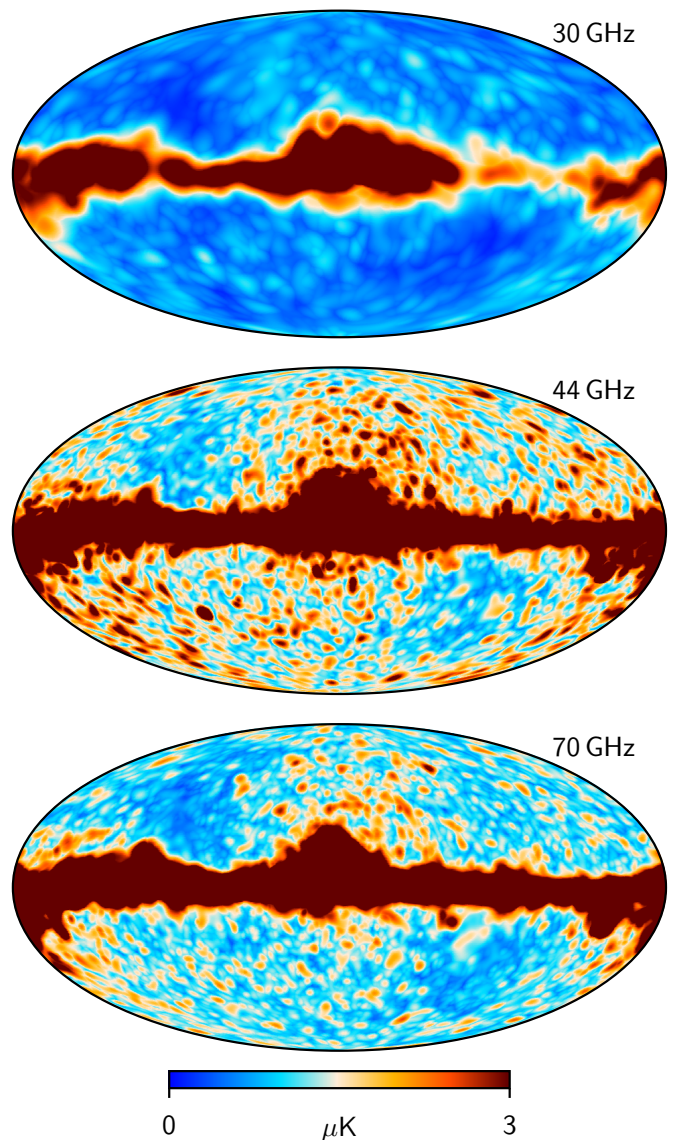
Fig. 5. Residual maps, $\boldsymbol{r}_\nu$, for each of the three *Planck* LFI frequencies, smoothed to a common angular resolution of 10° FWHM.
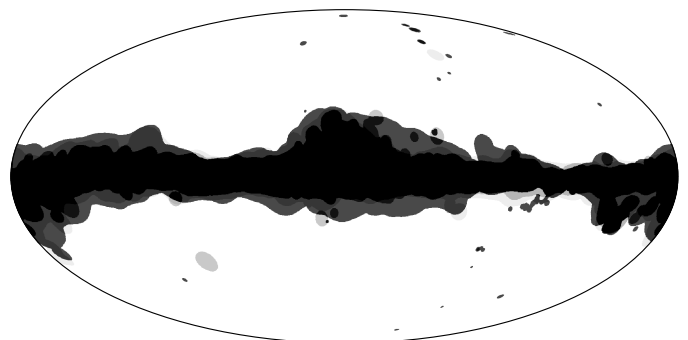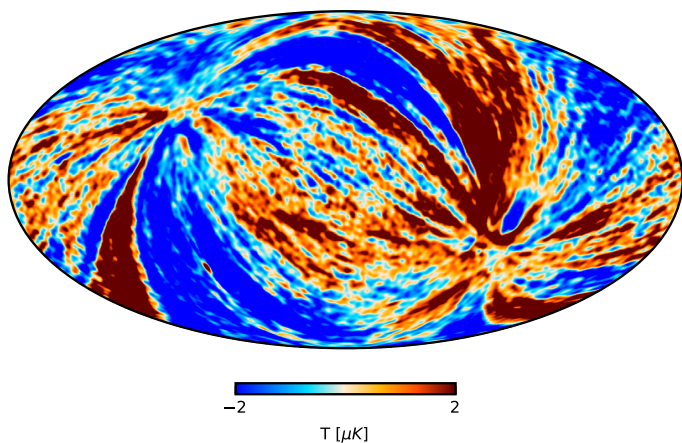

Fig. 6. Processing masks used for correlated noise sampling. Different shades of gray indicate different frequency masks. The allowed 30 GHz sky fraction (light) is $f_{\text{sky}} = 0.73$; the 44 GHz sky fraction (intermediate) is $f_{\text{sky}} = 0.81$; and the 70 GHz sky fraction (dark) is $f_{\text{sky}} = 0.77$.

Fig. 7. Correlated noise intensity sample for the 30 GHz band when fitting a model that assumes constant gains throughout the mission. Map has been smoothed to an angular resolution of 2.5° FWHM.
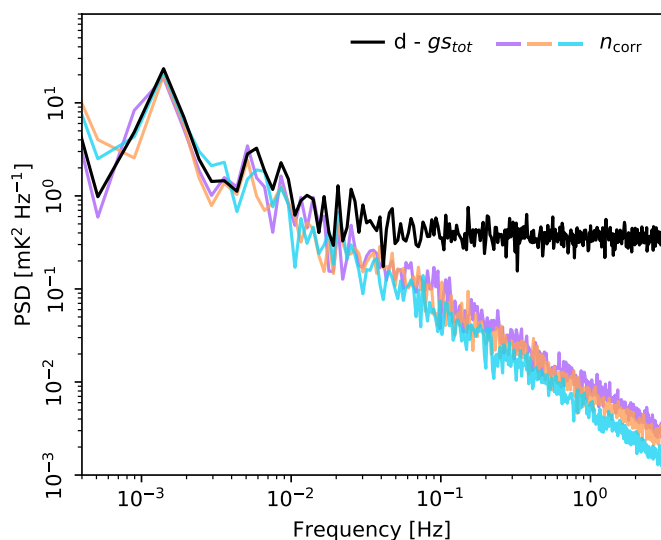
Fig. 8. Three subsequent samples (colored curves) of the correlated noise PSD for 25M, one of the 44 GHz radiometers. The black line shows the PSD of the signal-subtracted data.

residual, in the same manner as Galactic foregrounds described above, and this may therefore potentially also bias $\boldsymbol{n}^{\mathrm{corr}}$. Unlike the Galactic residuals, however, it is not possible to mask the CMB dipole, since it covers the full sky. The correlated noise component is therefore particularly susceptible to errors in either the gain or CMB dipole parameters, and residual large-scale dipole features in the binned $\boldsymbol{n}^{\mathrm{corr}}$ map is a classic indication of calibration errors. To illustrate the effect of an incorrect gain model, Fig. 7 shows a 30 GHz correlated noise sample when assuming that the gain is constant throughout the entire *Planck* mission.

The gain also has a direct connection with the white noise level, σ_0. This manifests itself in different ways, depending on the choice of units adopted for σ_0. When expressed in units of volts, the white noise level is simply given by the radiometer equation,

$$\sigma_0[\mathrm{V}] \propto g_{\mathrm{phys}} T_{\mathrm{sys}}, \tag{24}$$

Table 1. Distribution of posterior mean noise parameters for each radiometer. Error bars represent variation over time of the posterior mean values, and not the width of the posterior distribution for any given PID.

	Detector	α	f_{knee} [mHz]	σ_0 [mK]
30 GHz	27M	$-0.84^{+0.05}_{-0.06}$	210^{+22}_{-20}	$1.562^{+0.012}_{-0.012}$
	27S	$-0.84^{+0.06}_{-0.06}$	127^{+16}_{-12}	$1.708^{+0.010}_{-0.013}$
	28M	$-0.88^{+0.08}_{-0.11}$	137^{+22}_{-16}	$1.793^{+0.011}_{-0.013}$
	28S	$-1.00^{+0.11}_{-0.17}$	43^{+6}_{-5}	$1.638^{+0.008}_{-0.012}$
44 GHz	24M	$-1.03^{+0.10}_{-0.11}$	27^{+3}_{-3}	$3.155^{+0.012}_{-0.013}$
	24S	$-0.78^{+0.07}_{-0.07}$	92^{+29}_{-12}	$2.704^{+0.013}_{-0.018}$
	25M	$-1.02^{+0.11}_{-0.12}$	$19.5^{+2.7}_{-2.4}$	$2.832^{+0.010}_{-0.015}$
	25S	$-1.03^{+0.08}_{-0.08}$	45^{+5}_{-5}	$2.687^{+0.019}_{-0.015}$
	26M	$-0.97^{+0.07}_{-0.08}$	63^{+8}_{-5}	$3.264^{+0.018}_{-0.012}$
	26S	$-0.86^{+0.09}_{-0.09}$	50^{+8}_{-5}	$2.848^{+0.013}_{-0.012}$
70 GHz	18M	$-1.08^{+0.15}_{-0.19}$	$14.7^{+3.2}_{-2.3}$	$4.57^{+0.03}_{-0.03}$
	18S	$-1.18^{+0.16}_{-0.14}$	$18.2^{+3.3}_{-2.7}$	$4.18^{+0.02}_{-0.03}$
	19M	$-1.20^{+0.15}_{-0.16}$	$11.6^{+2.4}_{-1.8}$	$5.193^{+0.019}_{-0.036}$
	19S	$-1.10^{+0.13}_{-0.14}$	$13.7^{+2.5}_{-2.0}$	$4.962^{+0.018}_{-0.036}$
	20M	$-1.10^{+0.16}_{-0.23}$	$7.6^{+2.3}_{-1.4}$	$5.258^{+0.024}_{-0.028}$
	20S	$-1.25^{+0.13}_{-0.20}$	$5.5^{+1.8}_{-1.0}$	$5.571^{+0.014}_{-0.051}$
	21M	$-1.35^{+0.15}_{-0.12}$	38^{+8}_{-6}	$4.033^{+0.015}_{-0.016}$
	21S	$-1.15^{+0.15}_{-0.18}$	$13.0^{+2.7}_{-1.9}$	$5.018^{+0.027}_{-0.025}$
	22M	$-1.33^{+0.14}_{-0.23}$	$9.5^{+3.4}_{-2.1}$	$4.381^{+0.018}_{-0.019}$
	22S	$-1.25^{+0.21}_{-0.27}$	14^{+8}_{-5}	$4.746^{+0.024}_{-0.024}$
	23M	$-1.04^{+0.10}_{-0.12}$	30^{+4}_{-3}	$4.493^{+0.024}_{-0.021}$
	23S	$-1.19^{+0.08}_{-0.08}$	60^{+6}_{-6}	$4.815^{+0.019}_{-0.024}$

where g_{phys} is the actual physical gain of the radiometer, and T_{sys} is the system temperature (BeyondPlanck Collaboration 2020). In calibrated units of $\mathrm{K_{CMB}}$, however, the white noise level is

$$\sigma_0[\mathrm{K}] \propto \frac{g_{\mathrm{phys}}}{g_{\mathrm{model}}} T_{\mathrm{sys}}, \tag{25}$$

where g_{model} is the gain estimate in our model. When considering the evolution of the noise parameters as a function of time, we then note that $\sigma_0[\mathrm{V}]$ will correlate with the physical gain, which depends strongly on the thermal environment at any given time. On the other hand, if our gain model is correct, i.e., $g_{\mathrm{model}} \approx g_{\mathrm{phys}}$, these fluctuations will cancel in temperature units, and $\sigma_0[\mathrm{K}]$ should instead correlate with the system temperature, T_{sys}. The system temperature also depends on the physical temperature, T_{phys}, as the amplifiers' noise and waveguide losses increase with temperature. These were measured in pre-flight tests to be at a level $dT_{\mathrm{sys}}/dT_{\mathrm{phys}} \approx 0.2$–$0.5$ K/K, depending on the radiometer (Terenzi et al. 2009). In conclusion, if we observe a sudden change in $\sigma_0[\mathrm{K}]$ that is not present in $\sigma_0[\mathrm{V}]$, this might indicate a problem in the gain model. We also expect that changes in $\sigma_0[\mathrm{K}]$ reflect genuine variations of the white noise level, mainly driven by changes in the 20 K stage. In the following, we will plot σ_0 as a function of time in both units of volts and kelvins, and use these to disentangle gain and system temperature variations.
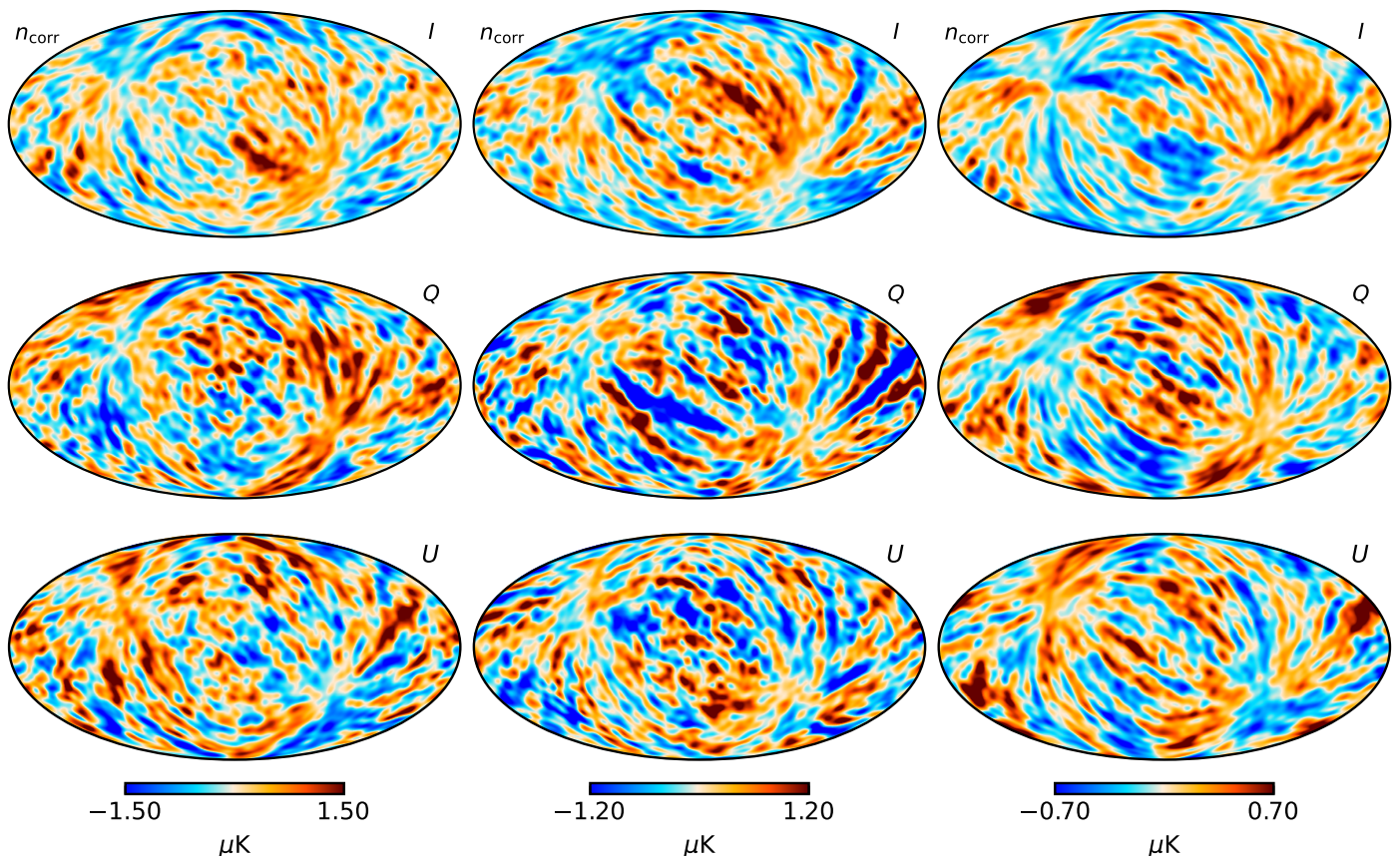
Fig. 9. Maps of a single Gibbs sample of the correlated noise added over all radiometers in the 30 GHz (left), 44 GHz (middle) and 70 GHz (right) bands. From top to bottom, rows show Stokes I, Q and U, respectively. Maps have been smoothed to a common angular resolution of 5° FWHM.

5. Results

We are now ready to present the main results obtained by applying the methods described above to the *Planck* LFI data within the BeyondPlanck Gibbs sampling framework (BeyondPlanck Collaboration 2020), as summarized in terms of the posterior distributions for each of the noise parameters. In total, six independent Gibbs chains were produced in the main BeyondPlanck analysis, each chain including 200 samples, for a total computational cost of about 230 000 CPU-hours or three weeks continuous wall-time (BeyondPlanck Collaboration 2020; Galloway et al. 2020a).

### 5.1. Posterior distributions and Gibbs chains

First, we recall that at every step in the Gibbs chain, we sample the correlated noise parameters for each pointing period and each radiometer, both the time-domain realization $\boldsymbol{n}^{\mathrm{corr}}$ and the PSD parameters ξ^n. To visually illustrate the resulting variations from sample to sample in terms of PSDs, Fig. 8 shows three subsequent spectrum samples for a single pointing period for the 25M radiometer. We see that the correlated noise follows the data closely at low frequencies, while at high frequencies the PSD is effectively extrapolated based on the current model. The scatter between the three colored curves shows the typical level of variations allowed by the combination of white noise and degeneracies with other parameters in the model.

Figure 9 shows the pixel-space correlated noise corresponding to a single Gibbs sample, obtained after binning $\boldsymbol{n}^{\mathrm{corr}}$ for all radiometers and all PIDs into an IQU map. Columns show

different frequency maps (30, 44, and 70 GHz), and rows show different Stokes parameters (I, Q, and U). Overall, we see that the morphology of each map is dominated by stripes along the *Planck* scanning strategy, as expected for correlated $1/f$ noise, and we do not see any obvious signatures of either residual foregrounds in the Galactic plane, nor CMB dipole leakage at high latitudes. This suggests that the combination of the data model and processing masks described above performs reasonably well. We also note that the peak-to-peak values of the total correlated noise maps are $O(1\,\mu\mathrm{K})$, which is of the same order of magnitude as the predicted signal from cosmic reionization (Planck Collaboration IV 2020). Thus, correlated noise estimation plays a critical role for large-scale polarization reconstruction, while it is negligible for CMB temperature analysis.

While the 30 and 70 GHz maps visually appear to be isotropic and random, we do see signatures of excess striping in the 44 GHz channel, in particular in Stokes Q. Several >1 μK stripes extend from the Eastern parts of the map, near the Galactic plane, through the Southern hemisphere. We have not yet been able to identify the origin of these stripes, but note that possible explanations include gain model errors for selected PID ranges, for instance in the form of one or more unmodelled amplifier gain jumps possibly triggered by thermal or electrical instabilities, or a sub-optimal processing mask. As reported by BeyondPlanck Collaboration (2020); Colombo et al. (2020); Paradiso et al. (2020), these artifacts lead to significant map-based χ^2 excesses in the final CMB polarization analysis, and thereby strongly limit our ability to constrain the optical depth of reionization with the current model. Our findings are consistent with
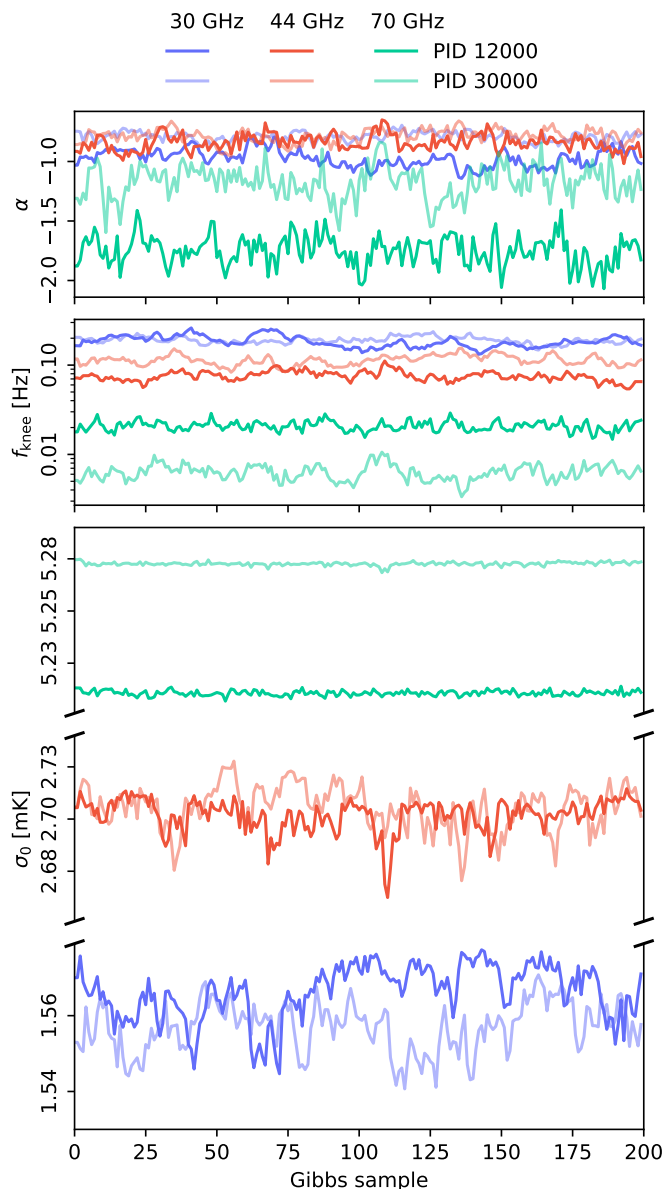
Fig. 10. Gibbs samples of noise parameters for two different PIDs for detectors 27M, 24S and 20M of the 30, 44 and 70 GHz bands respectively.

the difficulty experienced in treating the 44 GHz data for polarization analysis in all the official LFI DPC releases. However, the BeyondPlanck processing allows us to visually identify the structure of the excess correlated noise in the maps. Understanding the origin of these stripes and mitigating their impact represents a top priority for the next version of the BeyondPlanck processing.

For both n^{corr} and ξ^n, the main result of the BeyondPlanck pipeline are the full ensembles of Gibbs samples. These are too large to visualize in their entirety here, and are instead provided digitally, including animations of the correlated noise maps as a function of iteration.[4] In the following, we will therefore focus on ξ^n, and as an example Fig. 10 displays one of the full Gibbs chains for two different PIDs for one radiometer from each LFI frequency band. We see that the Gibbs chains appear both stable

---

[4] http://beyondplanck.science

---

and well-behaved. Some chains have longer Markov chain autocorrelation lengths than others, as expected from their different levels of degeneracies both within the noise model itself, and between the noise and the signal or gain. Overall, the Markov chain properties appear sound in all cases, with relatively short burnin and correlation lengths. We conservatively remove the first 50 samples from each chain to account for burn-in.

The main results are shown in Figs. 11–16, which summarize the noise PSD parameters for each LFI radiometer in terms of distributions of posterior means (top section; histograms made from the posterior means for all PIDs) and as average quantities as a function of PID (bottom section). The former are useful to obtain a quick overview of the mean behavior of a given radiometer, while the latter is useful to study its evolution in time. Blue, red, and green correspond to 30, 44, and 70 GHz radiometers, respectively. Mean ξ^n values are tabulated in Table 1, while the average noise properties of all radiometers in each band are plotted as a function of time in Fig. 17.

Regarding mean values, we see that the 30 GHz radiometers generally have fairly high knee frequencies, $f_{knee} \sim 100$ mHz, and shallow power law slopes, $\alpha \sim -0.85$. The 70 GHz channels, on the other hand, have lower knee frequencies, $f_{knee} \sim 20$ mHz, and steeper slopes, $\alpha \sim -1.2$. The 44 GHz channels generally fall between these two extremes.

The dashed lines in Figs. 11–16 show the *Planck* LFI DPC values for each parameter (Planck Collaboration II 2020), which are assumed to be constant throughout the mission. Generally speaking, these agree well with the results presented here. The main exception is the 30 GHz white noise level, σ_0, for which we on average find 2 % lower values. It is difficult to precisely pinpoint the origin of these differences, but we do note that Galactic foregrounds are particularly bright at 30 GHz. One possible hypothesis is therefore that these are fitted slightly better in the joint and iterative BeyondPlanck approach, as compared to the linear pipeline DPC approach.

5.2. Time variability and goodness-of-fit

Perhaps the single most important and visually immediate conclusion to be drawn from these plots is the fact that the noise properties of the LFI instrument vary significantly in time. This is evident in all three frequency channels and all radiometers. Furthermore, by comparing the time evolution between different radiometers, we observe many common features, both between frequencies and, in particular, among radiometers within the same frequency. Many of these may be associated with specific and known changes in the thermal environment of the satellite, and can be traced using thermometer housekeeping data; this will be a main topic for the next section.

The bottom panels in Figs. 11–16 show a χ^2 per PID of the following form,

$$\chi^2 \equiv \frac{\sum_{i=1}^{n_{samp}} \left(\frac{r_i}{\sigma_0}\right)^2 - n_{samp}}{\sqrt{2 n_{samp}}} \tag{26}$$

where n_{samp} is the number of samples, and r_i is the residual for sample i as defined by Eq. (23). Thus, this quantity measures the normalized mean-subtracted χ^2 for each PID, which should, for ideal data and $n_{samp} \gg 1$, be distributed according to a standard Gaussian distribution.

Starting with the 70 GHz channel, which generally is the most well-behaved, we see that the χ^2 fluctuates around zero for most channels, with a standard deviation of roughly unity.
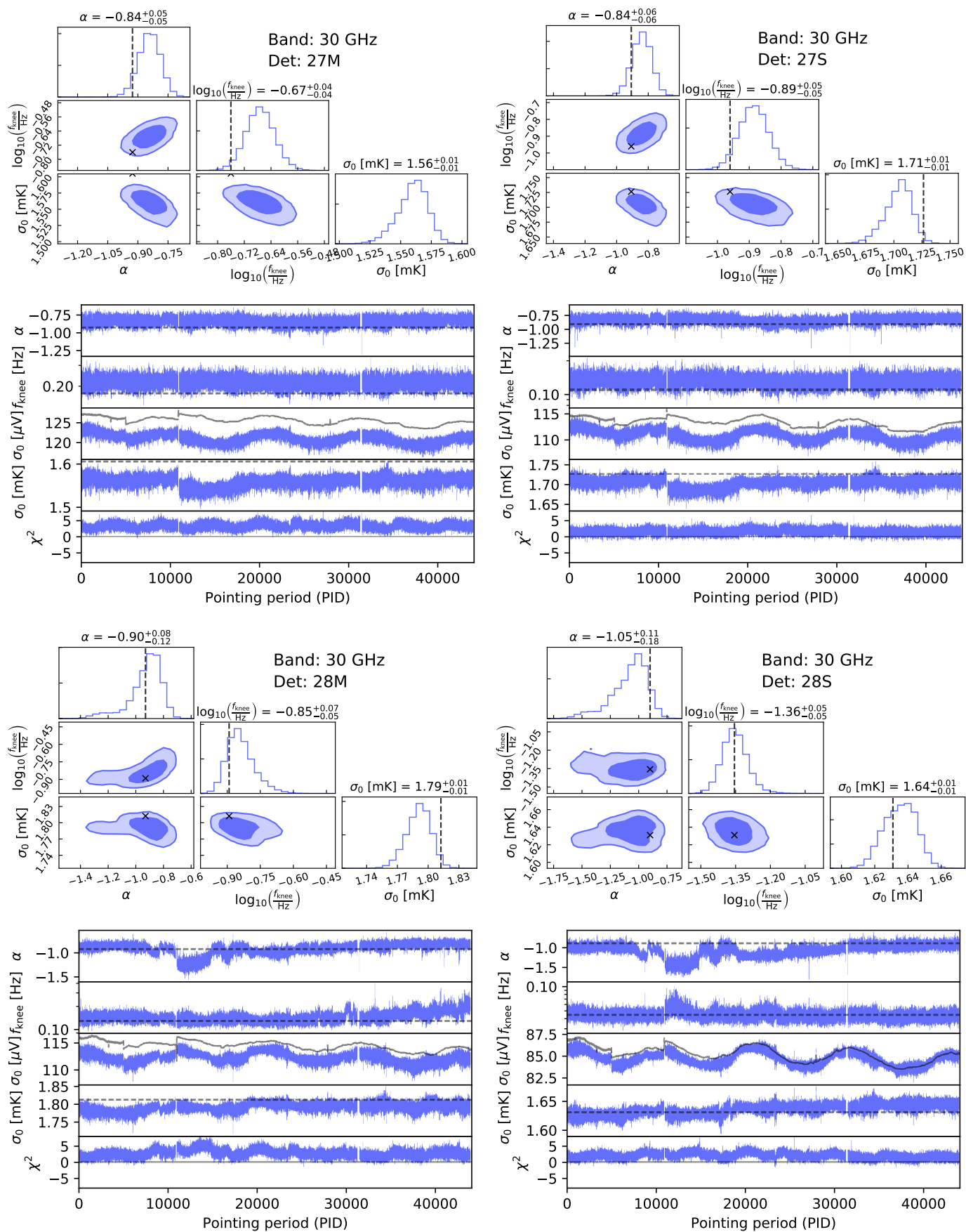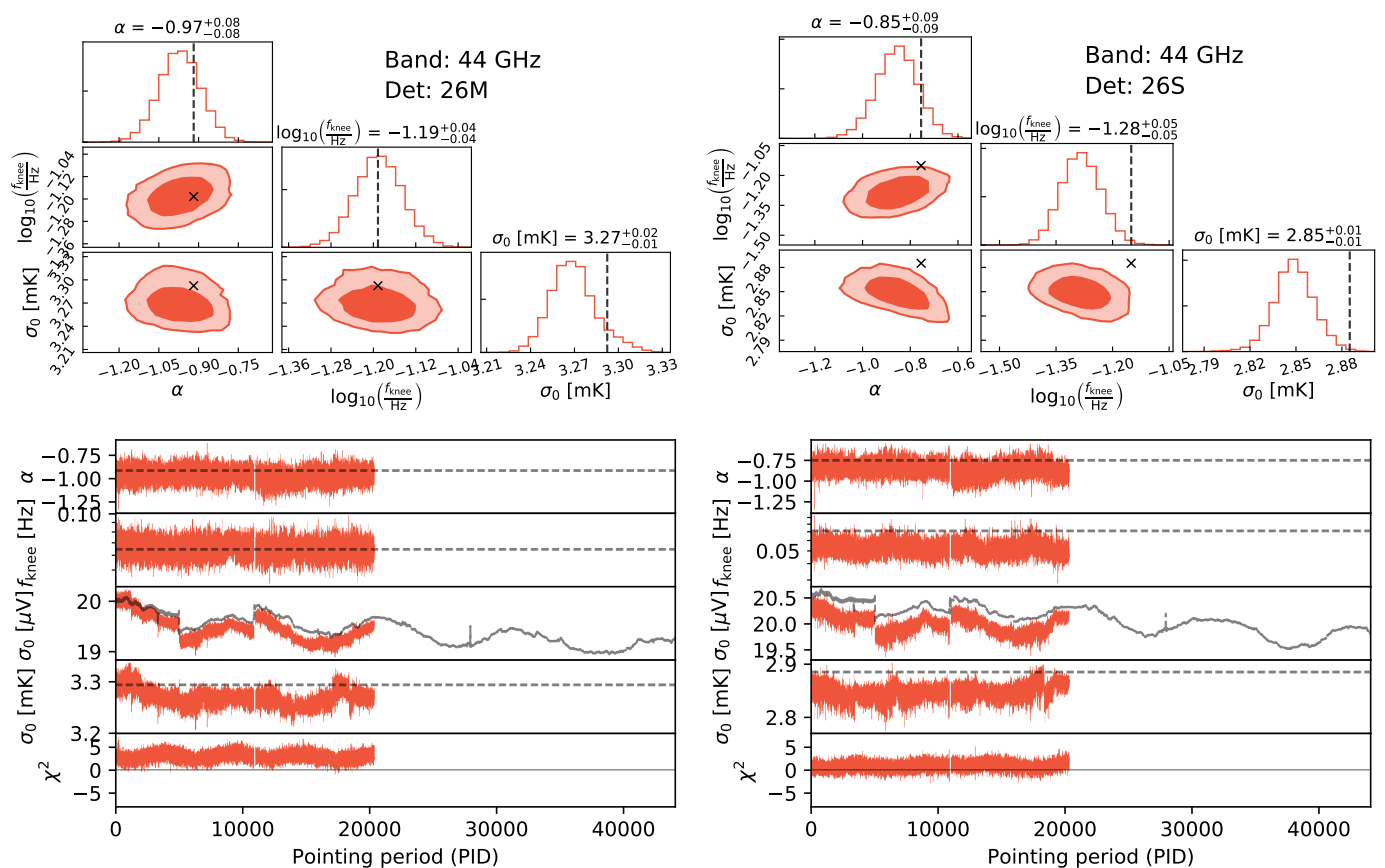
Fig. 11. Noise characterization of the *Planck* LFI 30 GHz radiometers; 27M (*top left*), 27S (*top right*); 28M (*bottom left*), and 28S (*bottom right*). For each radiometer, the top figure shows distributions of noise parameters PSD, $\xi^n = \{\sigma_0, f_{\text{knee}}, \alpha\}$, averaged over all Gibbs samples for the full mission. The bottom figure shows the time evolution of the posterior mean of the noise parameters, and the bottom panel shows the evolution in reduced normalized χ^2 in units of σ. Black dashed curves and crosses show corresponding values as derived by, and used in, the official *Planck* LFI DPC pipeline.
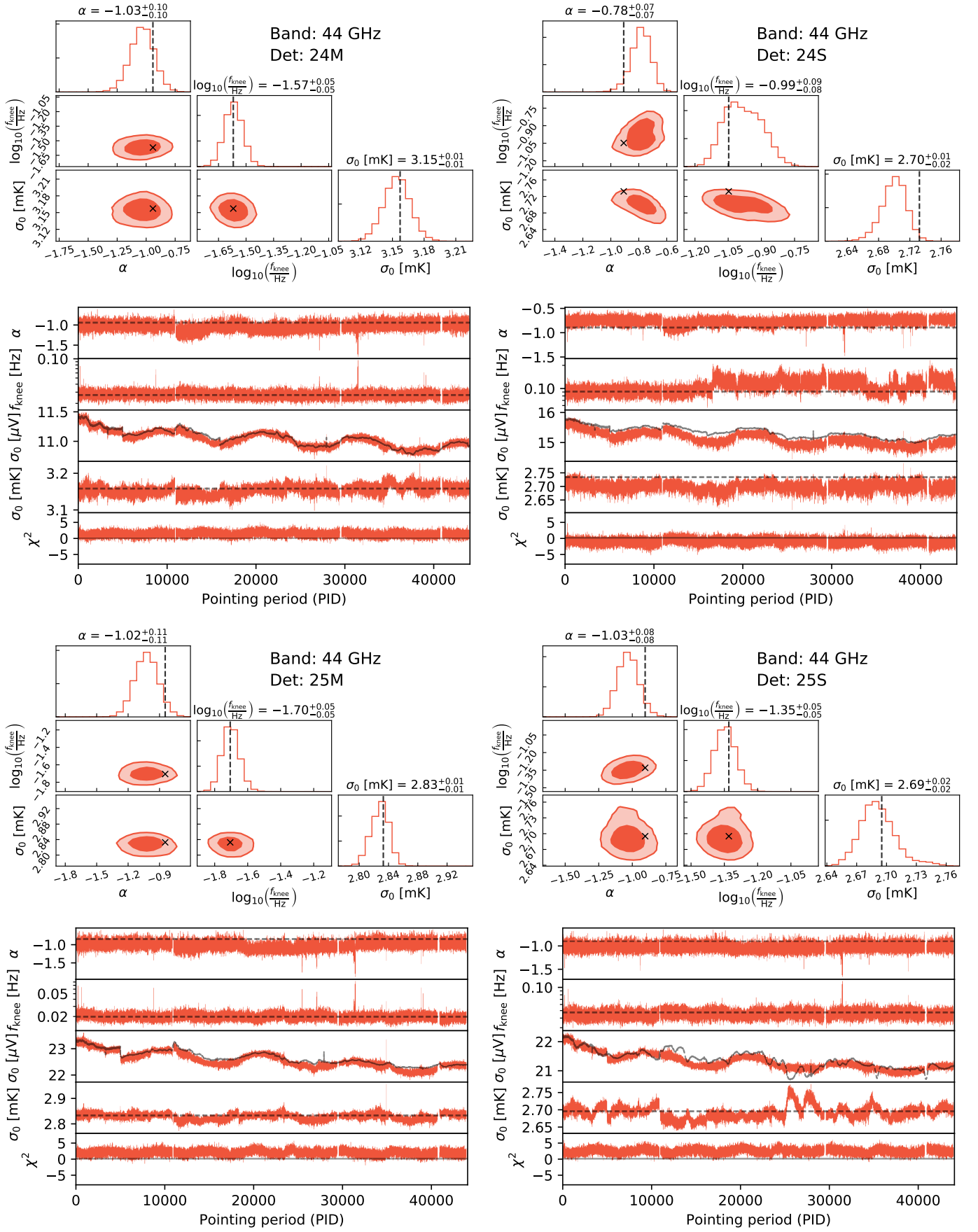
Fig. 12. Noise characterization of the *Planck* LFI 44 GHz radiometers; 24M (*top left*), 24S (*top right*); 25M (*bottom left*), and 25S (*bottom right*). For each radiometer, the top figure shows distributions of noise parameters PSD, $\xi^n = \{\sigma_0, f_{\text{knee}}, \alpha\}$, averaged over all Gibbs samples for the full mission. The bottom figure shows the time evolution of the posterior mean of the noise parameters, and the bottom panel shows the evolution in reduced normalized χ^2 in units of σ. Black dashed curves and crosses show corresponding values as derived by, and used in, the official *Planck* LFI DPC pipeline.

Fig. 13. Noise characterization of the *Planck* LFI 44 GHz radiometers; 26M (*left*), 26S (*right*). For each radiometer, the top figure shows distributions of noise parameters PSD, $\xi^n = \{\sigma_0, f_{knee}, \alpha\}$, averaged over all Gibbs samples for the full mission. The bottom figure shows the time evolution of the posterior mean of the noise parameters, and the bottom panel shows the evolution in reduced normalized χ^2 in units of σ. Black dashed curves and crosses show corresponding values as derived by, and used in, the official *Planck* LFI DPC pipeline.

The most notable feature is a short gap in the 18M and 18S radiometer distributions. As discussed by Suur-Uski et al. (2020), the χ^2 for these two radiometers shows an excess in this range, and these data are therefore omitted from the main analysis.

This is also the case for the 26M and 26S 44 GHz radiometers, to a higher extent. This particular case is considered explicitly in the next section, where it is shown that the 26S radiometer appears unstable for the second half of the mission, with significantly higher χ^2 and f_{knee} values. These data are therefore also removed from the main BEYONDPLANCK analysis (Suur-Uski et al. 2020).

In general, the 30 and 44 GHz channels appear less stable than the 70 GHz channels in terms of overall χ^2. These are neither centered on zero, nor stationary in time, but rather tend to show statistically significant excesses of 2–3 σ per PID, with internal temporal variations at the 1 σ level. These excesses will be discussed in Sect. 6, but we note for now that they must be expected to significantly impact higher-level analyses, in particular large-scale CMB polarization analysis, as they strongly suggest that a simple $1/f$ noise model is incomplete. As such, the predicted noise bias will necessarily be underestimated. Consequently, establishing a more complete noise model for the 30 and 44 GHz channels is a top priority for a next-generation BEYOND-PLANCK analysis.

As a typical illustration of such χ^2 failures, Fig. 18 shows the PSD for a range of 18 PIDs for the 28M 30 GHz radiometer. Here the $1/f$ model is not able to fit the real correlated noise to sufficient statistical accuracy at intermediate temporal frequen-

cies, between 0.1 and 10 Hz, but rather shows a generally flatter trend. Similar behavior is seen in most 30 and 44 GHz radiometers, while the 70 GHz radiometers are better behaved, probably simply because of their lower f_{knee} values.

Turning our attention to the ξ^n parameters, we see even larger variability than in the χ^2. First, we note a period of significant instability in most channels between PIDs 8–20 000, but most strikingly in the 70 GHz α estimates. This feature will be discussed in more detail in Sect. 6, where it is explicitly shown to be correlated with thermal variations. We note, however, that the $1/f$ noise model seems flexible enough to adjust to these particular changes, as no associated excess χ^2 is observed in the same range.

Next, when considering the white noise level, σ_0, given in units of volts or kelvins, we see the pattern anticipated in the previous section. The uncalibrated white noise in units of volts follows the slow drifts of the gain, which typically manifests itself in slow annual gain oscillations. In contrast, the calibrated noise in units of K_{CMB} is far more stable. An important exception to this is 25S, which exhibits large variations in K_{CMB}, in particular around PIDs 25–30 000. This might suggest a problem with the gain model for this particular radiometer, and this could possibly also be associated with the strong stripes in n^{corr} noted above.

Other significant features include sharp jumps in f_{knee}, for instance as seen in 24S. These typically coincide with external events, for instance during cooler maintainence (see Sect. 6 and Gjerløw et al. 2020).
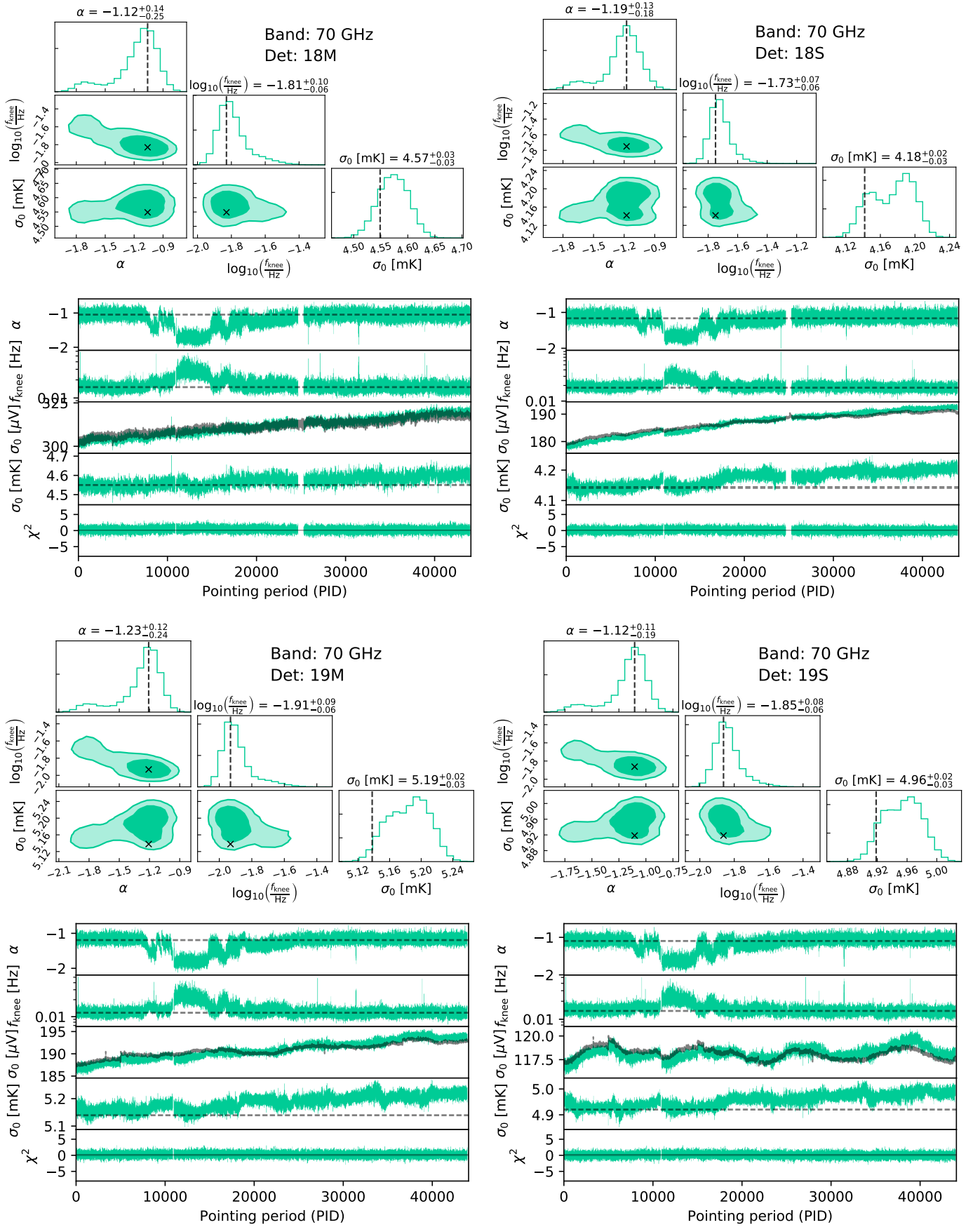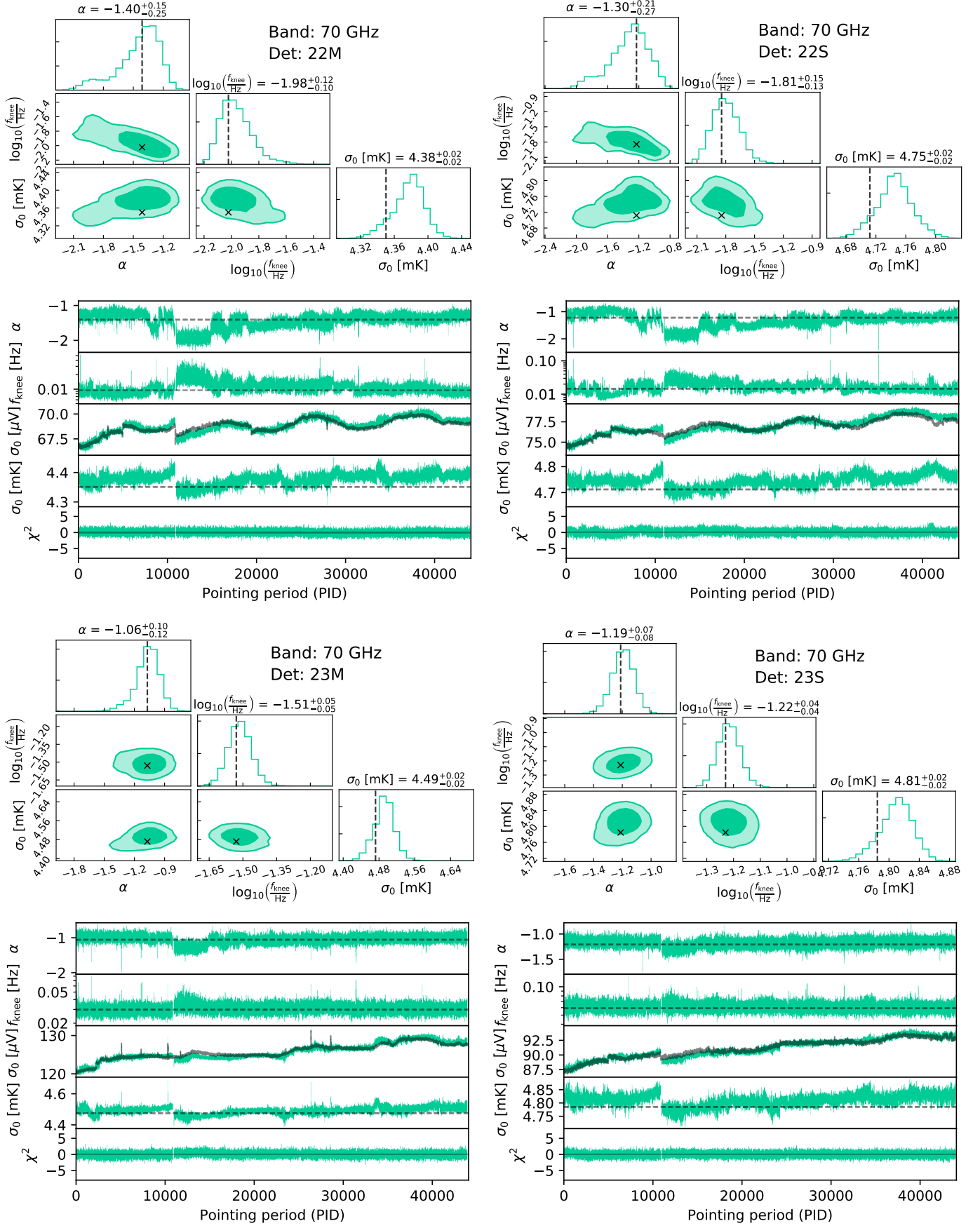
Fig. 14. Noise characterization of the *Planck* LFI 70 GHz radiometers; 18M (*top left*), 18S (*top right*); 19M (*bottom left*), and 19S (*bottom right*). For each radiometer, the top figure shows distributions of noise parameters PSD, $\xi^n = \{\sigma_0, f_{\text{knee}}, \alpha\}$, averaged over all Gibbs samples for the full mission. The bottom figure shows the time evolution of the posterior mean of the noise parameters, and the bottom panel shows the evolution in reduced normalized χ^2 in units of σ. Black dashed curves and crosses show corresponding values as derived by, and used in, the official *Planck* LFI DPC pipeline.
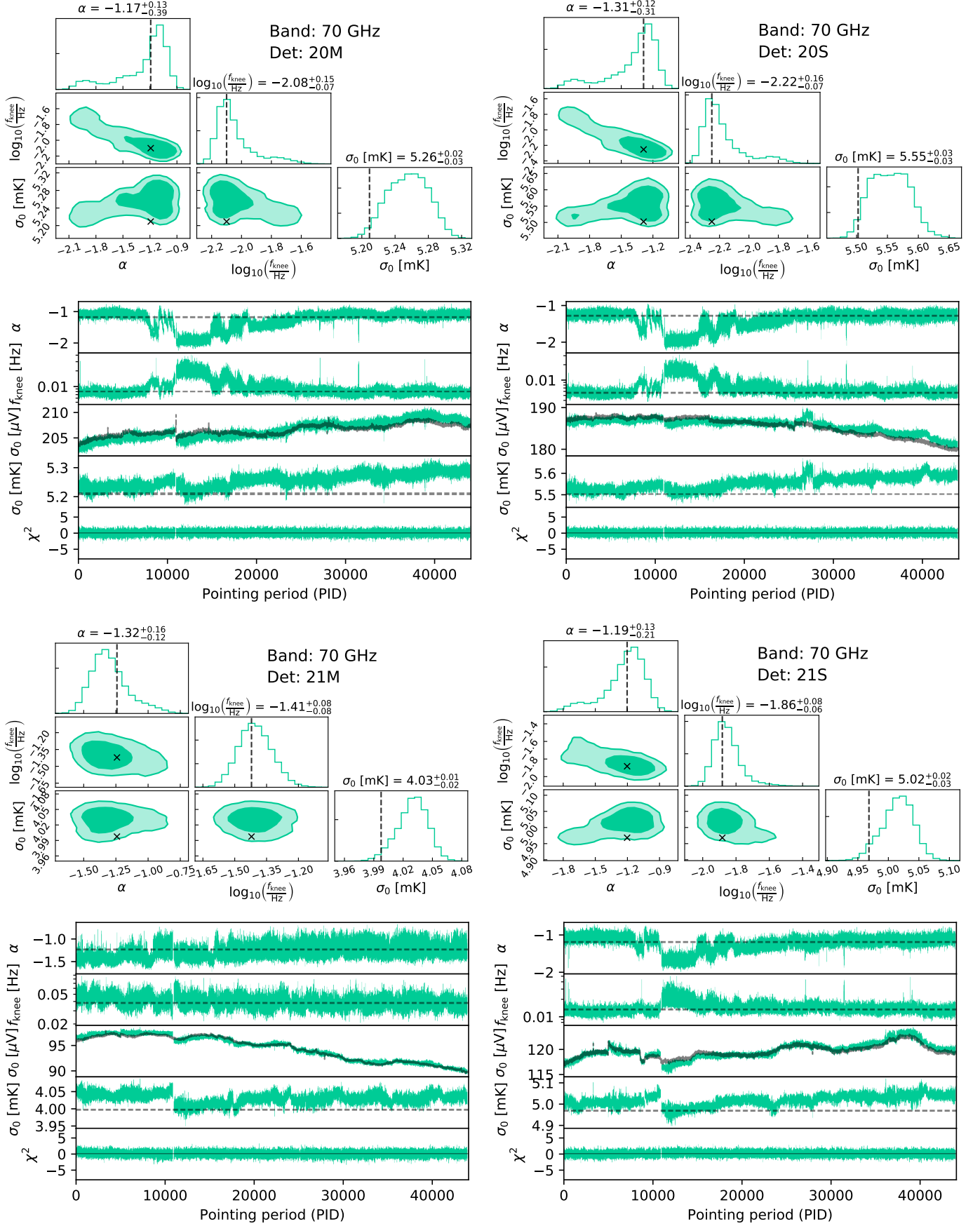
Fig. 15. Noise characterization of the *Planck* LFI 70 GHz radiometers; 20M (*top left*), 20S (*top right*); 21M (*bottom left*), and 21S (*bottom right*). For each radiometer, the top figure shows distributions of noise parameters PSD, $\xi^n = \{\sigma_0, f_{knee}, \alpha\}$, averaged over all Gibbs samples for the full mission. The bottom figure shows the time evolution of the posterior mean of the noise parameters, and the bottom panel shows the evolution in reduced normalized χ^2 in units of σ. Black dashed curves and crosses show corresponding values as derived by, and used in, the official *Planck* LFI DPC pipeline.

Fig. 16. Noise characterization of the *Planck* LFI 70 GHz radiometers; 22M (*top left*), 22S (*top right*); 23M (*bottom left*), and 23S (*bottom right*). For each radiometer, the top figure shows distributions of noise parameters PSD, $\xi^n = \{\sigma_0, f_{\text{knee}}, \alpha\}$, averaged over all Gibbs samples for the full mission. The bottom figure shows the time evolution of the posterior mean of the noise parameters, and the bottom panel shows the evolution in reduced normalized χ^2 in units of σ. Black dashed curves and crosses show corresponding values as derived by, and used in, the official *Planck* LFI DPC pipeline.
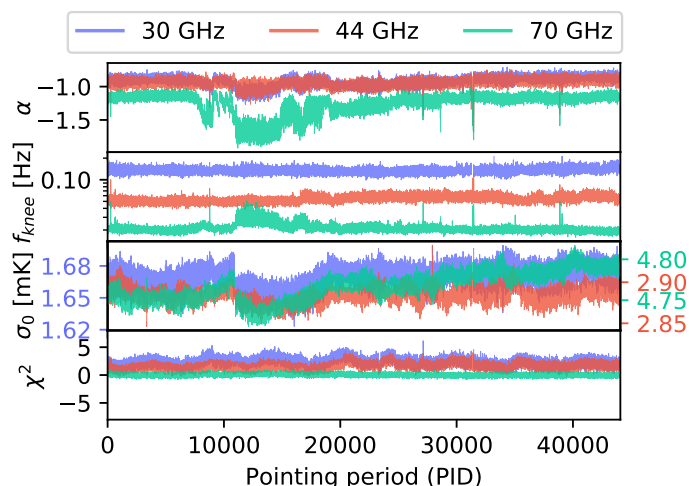
Fig. 17. Posterior mean noise parameters averaged over all radiometers in each band, for the full mission.
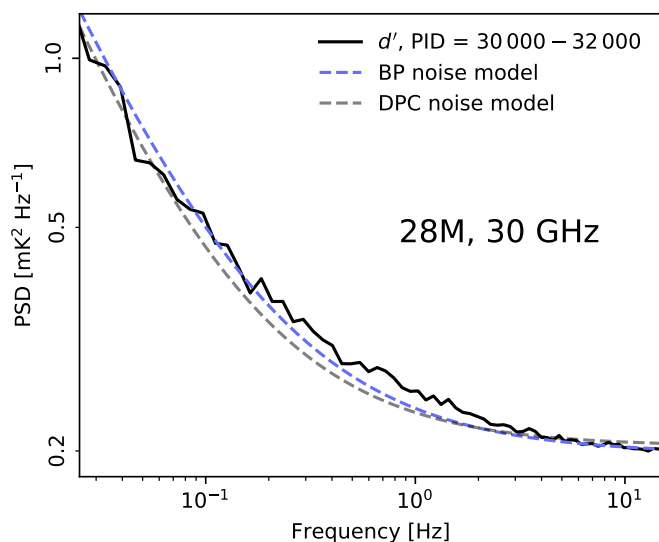
Fig. 18. PSD of signal-subtracted data from radiometer 28M, averaged over 18 PIDs (at intervals of 100 PIDs) in the range 30 000–32 000 (black). The dashed lines show the mean BEYONDPLANCK (dashed blue) and LFI DPC (dashed gray) noise models for the same data. An excess is seen at intermediate frequencies between 0.1 and 10 Hz.

6. Systematic effects

Previous LFI analyses have assumed a stationary noise model with three fixed parameters (σ_0 [K], f_{knee}, and α) for each of the 22 radiometers. In contrast, each of these parameters is in BEYONDPLANCK estimated for every PID, increasing the total number of PSD noise parameters from 66 to about 3 million. This increase of information allows us to capture the effects of evolution in the radiometer responses and local thermal environment, as well as subtle interactions between them. In this section, we will use this new information to characterize potential residual systematic effects in the data, and, as far as possible, associate these with independent housekeeping data or known satellite events. An overview of the measurements from eight temperature sensors that are particularly important for LFI is provided in Fig. 19.
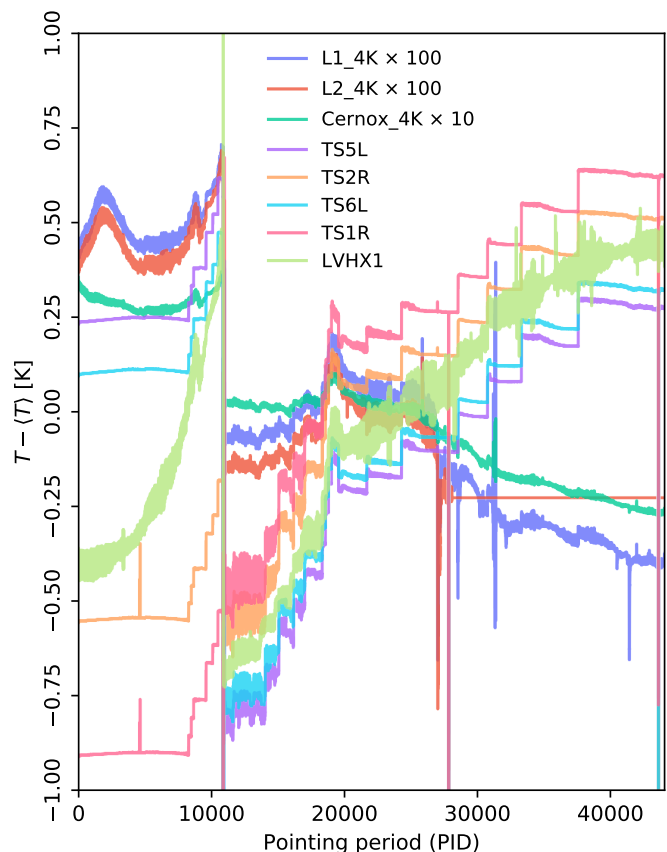
Fig. 19. High-level comparison of measurements from eight temperature sensors that are particularly relevant for LFI. Sensors TS5L, TS6L, TS1R, TS2R are installed in the 20 K focal plane frame, while LVHX1 is the liquid-vapour heat exchanger providing 18K to HFI; sensors L1_4K, L2_4K and Cernox_4K are on the HFI 4 K stage supporting the LFI 4 K reference loads. The step-like increases in the 20 K stage are visible both before and after the sorption cooler switchover event (near PID 11 000). For details on the locations of the various temperature sensors, see Fig. 21 of Bersanelli et al. (2010) and Fig. 18 of Lamarre et al. (2010). For visualization purposes, the mean value has been subtracted from each data set, and some have been scaled by one or two orders of magnitude, as indicated in the legend.

For details on the locations of the various temperature sensors, see Fig. 21 of Bersanelli et al. (2010) and Fig. 18 of Lamarre et al. (2010).

6.1. Temperature changes in the 20 K stage

A key element for the LFI thermal environment was the *Planck* sorption cooler system (SCS), which provided the 20 K stage to the LFI front-end and the 18K pre-cooling stage to HFI. The SCS included a nominal and a redundant unit (Planck Collaboration II 2011). In August 2010 (around PID 11 000), a heat switch of the nominal cooler unit reached its end-of-life, and the SCS was therefore switched over to the redundant cooler.[5] This "switchover" event implied a major redistribution of the temperatures in the LFI focal plane, with variations at ~1 K level, for two main reasons. First, the efficiency of the newly active redundant cooler led to an overall decrease of the absolute tempera-

---

[5] This operation took place at PID 10911, corresponding to Operation Day (OD) 454.
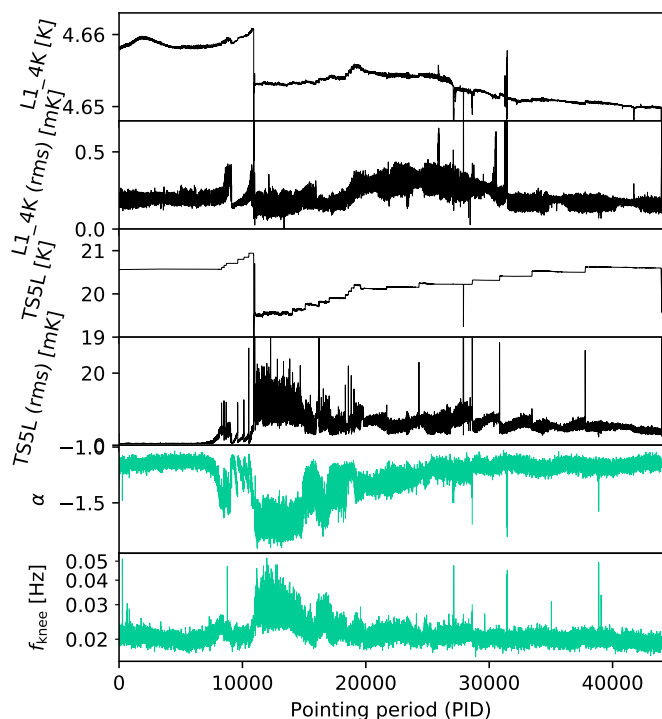
Fig. 20. Average correlated noise properties of the 70 GHz radiometers (bottom two panels) compared with 4 K and 20 K temperature sensor read-outs (top four panels) for the full mission.

Fig. 21. Same as Fig. 20, but zoomed in on PIDs 7000–11 000.

ture. Second, because of the different location of the interface between the focal plane structure and the cold-end for the redundant cooler, a change of temperature gradients appeared across the focal plane.

Since the SCS dissipated significant power, changes in its configuration produced measurable thermal effects in the entire *Planck* spacecraft, and most directly in the 20 K stage. In the period preceding the switchover, starting around PID 8000, a series of power input adjustments were commanded to reduce thermal fluctuations in the 20 K stage while optimizing the sorption cooler lifetime, which generated a number of step-like increases in the LFI focal plane temperature. These are measured by all the LFI temperature sensors located in the 20 K focal plane unit, as shown in Fig. 19.

Following the switchover, in the period with PIDs 11–15 000, a significant increase of 20 K temperature fluctuations was observed. These excess fluctuations were understood as due to residual liquid hydrogen sloshing in the inactive cooler and affecting the cold-end temperature. The issue was resolved by heating the unit and letting the residual hydrogen evaporate. Afterwards, to optimize the performance and lifetime of the operating cooler, several periodic, step-like adjustments were again introduced in the operational parameters of the cooler. This resulted in a semi-gradual, monotonic increase of the LFI focal plane temperature from switchover to end of mission of ∼1.3 K.

In Fig. 19 the sudden discontinuity at switchover (PID 11 000) is visible for all temperature sensors, and the stepwise up-ward trend driven by SCS operational adjustments can be seen in all 20 K sensors. These temperature variations directly affected the LFI noise performance for most radiometers, as observed in the lower panels of Figs. 11–16. To see this, it may be useful to concentrate on a well-behaved case (e.g., radiometers
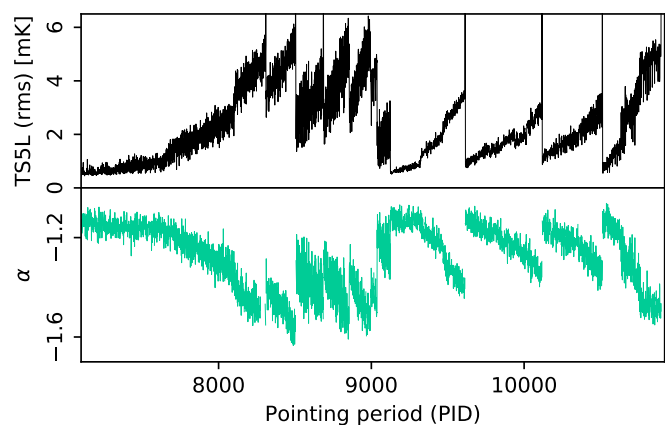
22 or 23, Fig. 16) and then recognize the same features in other radiometers.

The effect of the SCS switchover shows up as a sharp discontinuity also in the white noise levels near PID 11 000. The sudden decrease of the focal plane temperature of about 1 K implies a change in radiometer gain, as well as a genuine reduction in radiometer noise. This leads to a decrease not only of σ_0 [V] but also of σ_0 [K]. Furthermore, due to the change in cold-end interface, the temperature drop at switchover was larger on the top-right-hand side of the focal plane (as defined by the view in Fig. 6 of BeyondPlanck Collaboration 2020) than in other regions. In particuclar, we see in Figs. 11–16 that the drop in σ_0 [K] is particularly pronounced for radiometers 21, 22, 23, 27 (both M and S), which are all located in that portion of the focal plane.

Using again Fig. 16 as a guide, we can also recognize the effect of the incremental increase of focal plane temperature due to sorption cooler adjustments, both before and after switchover. The increasing physical temperature of the focal plane drives a corresponding increase of σ_0 [K], which is visible for most of the radiometers in Figs. 11–16. However, we cannot exclude that part of the observed slow increase of white noise is due to aging effects degrading the intrinsic noise performance of the front-end amplifiers. To disentangle these two components would require a more detailed thermal and radiometric model.

6.2. Temperature fluctuations and $1/f$ parameters

In Fig. 20 (top four panels) we report the value and rms of representative temperature sensor of the 4 K and 20 K stages (L1_4K and TS5L). During the thermal instability period that followed the switchover, the noise properties of essentially all the 70 GHz radiometers markedly changed their $1/f$ noise behavior (with the only notable exception of 21M). This is highlighted in the lower two panels of Fig. 20, which show the averaged values of α and f_{knee} for all the 70 GHz radiometers. The correlation between $1/f$ noise parameters and temperature fluctuations is excellent, with higher fluctuations producing an increase in f_{knee} and a steepening (i.e., more negative) slope α. The latter is a typical behavior of thermally driven instabilities, which tend to transfer more power to low frequencies, and thus steepen the $1/f$ tail. This behavior shows up also in the individual 70 GHz radiometers (Figs. 14–16).
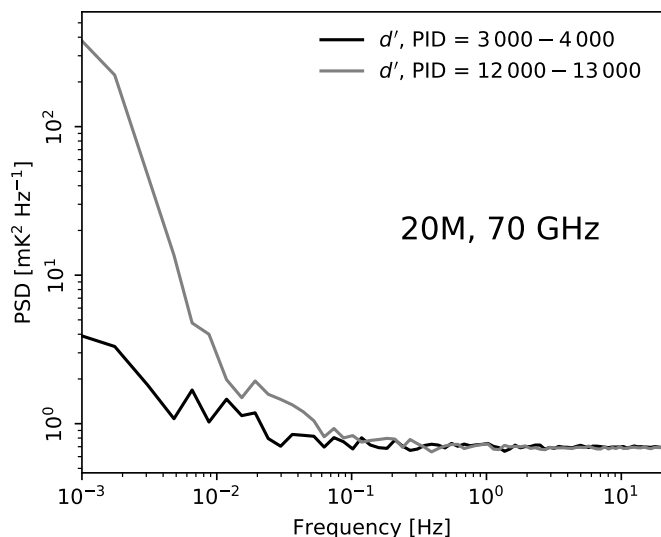
Fig. 22. PSD of signal subtracted data from radiometer 20M, averaged over 10 PIDs in the ranges 3000–4000 (black) and 12 000–13 000 (grey).

Figure 21 is a zoom into the pre-switchover period (PID 7000–11 000) of the upper plot. Here we see the effect of some of the step-wise adjustments in the sorption cooler operation, whose main effect is to temporarily reduce the temperature fluctuations. The observed tight correlation with the steepening of the slope is striking.

For a specific example of how noise property variations modify the noise PSD, Fig. 22 shows the average PSD for 10 PIDs between 3000–4000 (black) compared to 10 PIDs between 12 000–13 000 (grey) for the 70 GHz 20M radiometer. We see large increases in power at low frequencies, and a shift in the knee frequency.

These correlations appear more weakly in the 30 and 44 GHz radiometers (see Fig. 17). In particular, there is no correlation with the knee frequency. This behavior could be partly explained by the fact that, by mechanical design, the front-end modules (FEMs) of the 30 and 44 GHz are less thermally coupled to the frame and cooler front-end; or it could be indicative of an additional source of non-thermal correlated noise that dominates the slope and knee frequency of these channels. This could be the case also for the 70 GHz radiometer 21M, for which the lack of correlation cannot be explained in terms of poor thermal coupling.

These hypotheses are supported by Fig. 18, which compared the PSD of the 30 GHz 28M signal-subtracted data, averaged over 18 PIDs in a typical stable period, with both the Beyond-Planck and LFI DPC noise models for the same period. None of the models are able to properly describe the observed data. The deviation indicates that there is an excess power in the frequency range between 0.1 and 5 Hz.

6.3. Seasonal effects and slow drifts

The changing Sun-satellite distance during the yearly *Planck* orbit around the Sun produced a seasonal modulation of the solar power absorbed by the spacecraft. The corresponding effect on the LFI thermal environment was negligible for the actively-controlled front end, as demonstrated by the lack of yearly modulation in the 20 K temperature sensors (see Fig. 19 and upper

panel of Fig. 20). However, the 300 K environment and the passive cooling elements (V-groove radiators) were affected by a ~1 % seasonal modulation (see Fig. 6 of Planck Collaboration I 2014).

Since the radiometer back-end modules (BEMs) provided a major contribution to the radiometer gain g, and these are located in the 300 K service module (SVM), the thermal susceptibility of the BEMs coupled with local thermal changes is expected to induce radiometer gain variations. On the other hand, since the BEMs are downstream relative to the >30 dB amplification from the FEMs, their contribution to the noise temperature, T_{sys}, is negligible. Therefore we may expect the LFI uncalibrated signal (and the uncalibrated noise σ_0 [V]) to show a seasonal modulation due to thermally-driven BEM gain variations, with essentially no degeneracy with T_{sys}.

Figures 11–16 show that several LFI radiometers exhibit such modulation in the uncalibrated white noise, σ_0 [V], throughout the four year survey. For all of these, the modulation disappears in σ_0 [K], indicating that our gain model properly captures this effect. We also observe that the sign of the modulation is opposite for the 70 GHz and the 30–44 GHz radiometers. Furthermore, all radiometers that exhibit seasonal modulation also show a systematic slow drift of σ_0 [V] throughout the mission with the same sign as the initial modulation (which corresponds to increasing physical temperatures in the SVM). Since the spacecraft housekeeping recorded a slow overall increase in temperature throughout the mission ($\Delta T \approx 5$ K), the observed drift of σ_0 [V] is qualitatively consistent with the hypothesis of BEM susceptibility as the origin of the effect.

For each radiometer, the amplitude of the modulation depends on the details of the thermal susceptibility of the LFI elements down-stream relative to the third V-groove, including waveguide losses, BEM components, particularly low-noise amplifiers (LNAs), detector diodes, data acquisition electronics (gain and offset), etc. The dominant element is the BEM, whose thermal susceptibility was measured in the LFI pre-launch test campaign for the 30 and 44 GHz radiometers (Villa et al. 2010). The change in BEM output voltage, ΔV_{out}, as a function of the variation in BEM physical temperature, ΔT_{BEM}, can be written as

$$\Delta V_{\text{out}} \propto \phi_{\text{BEM}} \Delta T_{\text{BEM}} \left(T_{\text{sys}} + T_{\text{in}} \right), \tag{27}$$

where T_{in} is the input signal temperature (either sky or reference load) and ϕ_{BEM} is a transfer function quantifying the BEM thermal susceptibility. The measured values of ϕ_{BEM} (Villa et al. 2010) were slightly negative for all the 30 and 44 GHz radiometers, ranging from −0.01 to −0.02, and this is consistent with both the observed overall drift and the seasonal effect. No such ground tests could be done for the 70 GHz instrument. However, in-flight tests during commissioning (Cuttaia & Terenzi 2011) revealed that the sign of ϕ_{BEM} for the 70 GHz radiometers was opposite to those of 30 and 44 GHz, which is consistent with our interpretation.

6.4. Inter-radiometer correlations

So far, we have mostly considered noise properties as measured separately for each radiometer. However, given the significant sensitivity to external environment parameters discussed above, it is also interesting to quantify correlations between detectors. As a first measure of this, we plot in Fig. 23 the cross-correlation of $\boldsymbol{n}_{\text{corr}}$ averaged over all pairs of radiometers within each frequency band as a function of PID. As expected from the previous
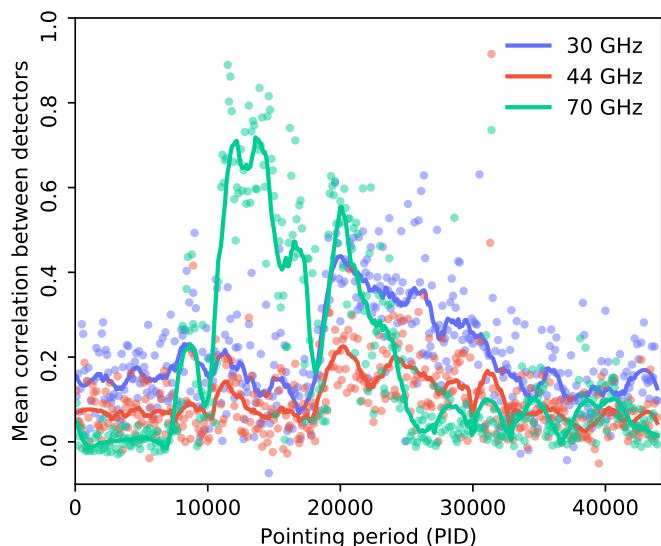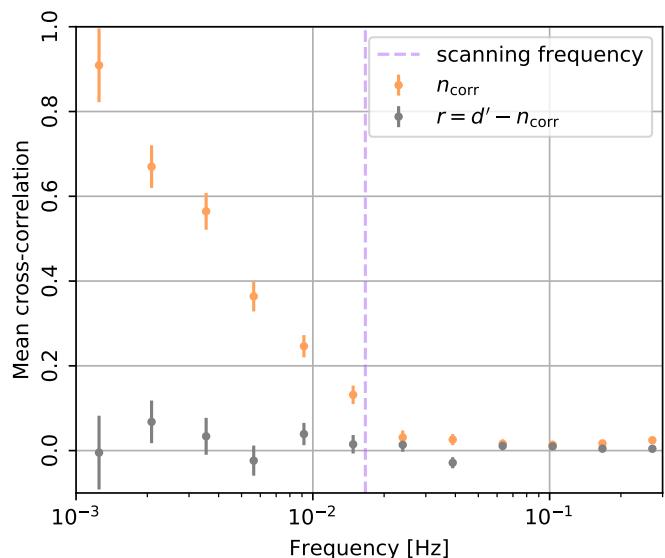
Fig. 23. Average correlation between the correlated noise in the different radiometers in each frequency band for the full mission.
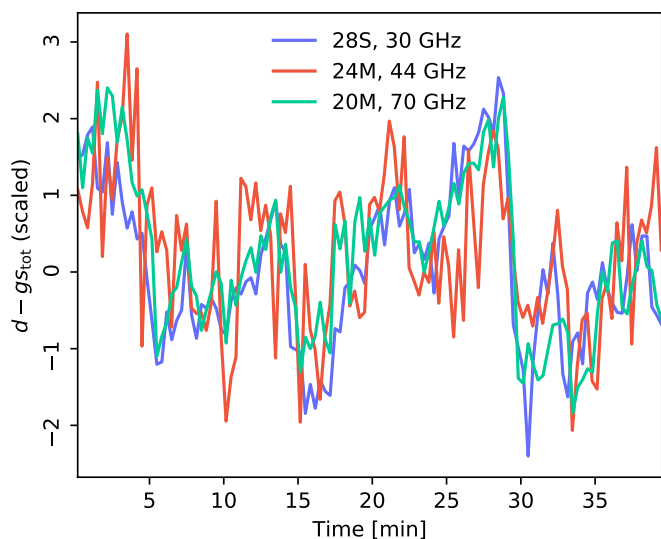
Fig. 24. Signal subtracted data from radiometers from all three bands for PID 12 301. The data is averaged over a 20 second timescale and scaled to fit in the same plot.

discussion, we find a large common correlation for the 70 GHz channel that peaks in the post-switchover period. Similar coherent patterns are seen in the 30 and 44 GHz channels, but at somewhat lower levels.

As a specific example of such common mode noise, Fig. 24 shows the signal subtracted timestreams for one radiometer from each band for PID 12 301, which is representative for the period of maximum correlation. Here we see that the same large scale fluctuations are present in all three bands. In Fig. 25 we show the average cross correlation between time streams of all 70 GHz radiometers for the same PID. We compare the average correlation between the correlated noise components, n_{corr}, with the correlation between the residuals, $d' - n_{\text{corr}}$. We see that even though the correlations between the n_{corr} components are large, the residuals are highly uncorrelated. This is an indication


Fig. 25. Average cross correlation between timestreams of all 70 GHz radiometers for PID 12301. Orange points show average correlation between the correlated noise components, while the grey points shows average correlation between the residuals. We see that even though the correlation between the correlated noise components is large, the residuals are completely uncorrelated, indicating that this correlated signal does not leak into the rest of the pipeline, but is all incorporated into the correlated noise.

that the common mode signal is efficiently described by n_{corr}, and it therefore does not leak into the rest of the BeyondPlanck pipeline.

Figure 26 shows a global correlation matrix of all the noise parameters for all the LFI radiometers throughout the mission. A number of interesting features can be recognized in this diagram:

1. We note that all 70 GHz radiometers exhibit an internally coherent trend, where f_{knee} and α behave essentially as a common mode for the entire 70 GHz array, with the only exception being 21M. This coherent behavior reflects the common thermal origin of the $1/f$ noise of the 70 GHz radiometers, as discussed in Sect. 6.2. We also see that σ_0 [K] shows a similar common mode behavior for the 70 GHz radiometers and, to a lesser extent, it correlates also with the σ_0 [K] of the 44 and 30 GHz radiometers. This is indicative of the fact that changes in the LFI radiometers' sensitivity are driven by the global LFI thermal environment, most importantly by the slow increase in temperature at the 20 K temperature stage.

2. For 30 and 44 GHz we do not observe the same common mode behavior for f_{knee} and α as for the 70 GHz. Rather, we see positive correlation (red pixels in Fig. 26) between f_{knee} and α within each single radiometer. This suggests that (a) the dominant source of $1/f$ noise is independent for each 30 and 44 GHz radiometers, and (b) for a given radiometer, as f_{knee} increases, the slope becomes flatter (i.e., α becomes less negative). This behavior further supports the hypothesis that the dominant source of correlated noise in the 30 and 44 GHz is not of thermal origin.

3. Finally, we observe an anti-correlation between f_{knee} and σ_0 (as a common mode at 70 GHz and individually for 30 and 44 GHz). Slightly larger values of f_{knee} for lower σ_0 can be understood in terms of the correlated fluctuations becoming subdominant near f_{knee} when the white noise increases during the mission time.
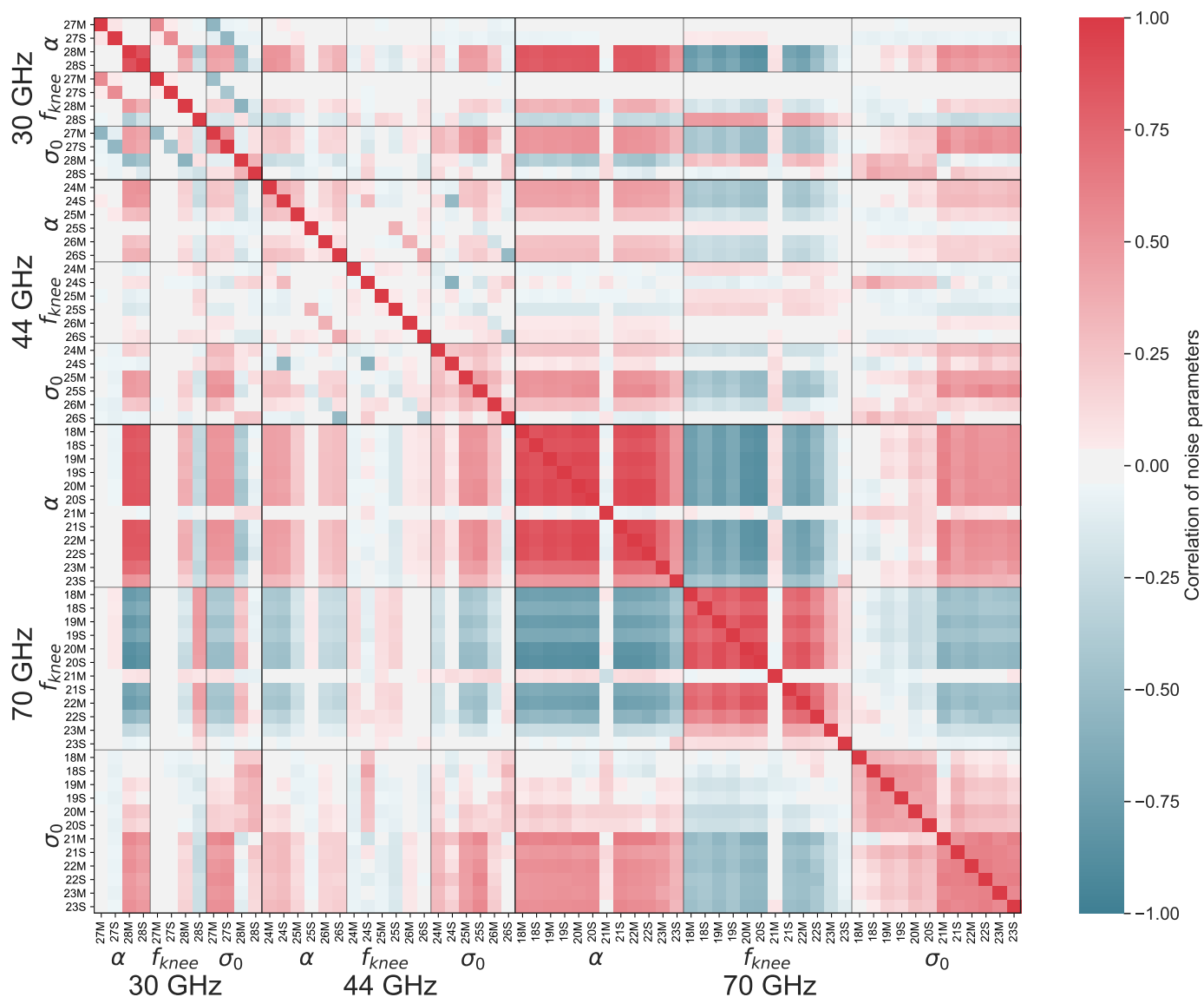
Fig. 26. Average over all Gibbs samples of the noise parameters, $\xi^n = \{\sigma_0, f_{knee}, \alpha\}$, for each PID. We then find the correlation in time between these averages for the different bands and detectors. The results here are for the calibrated white noise level, σ_0 [K].
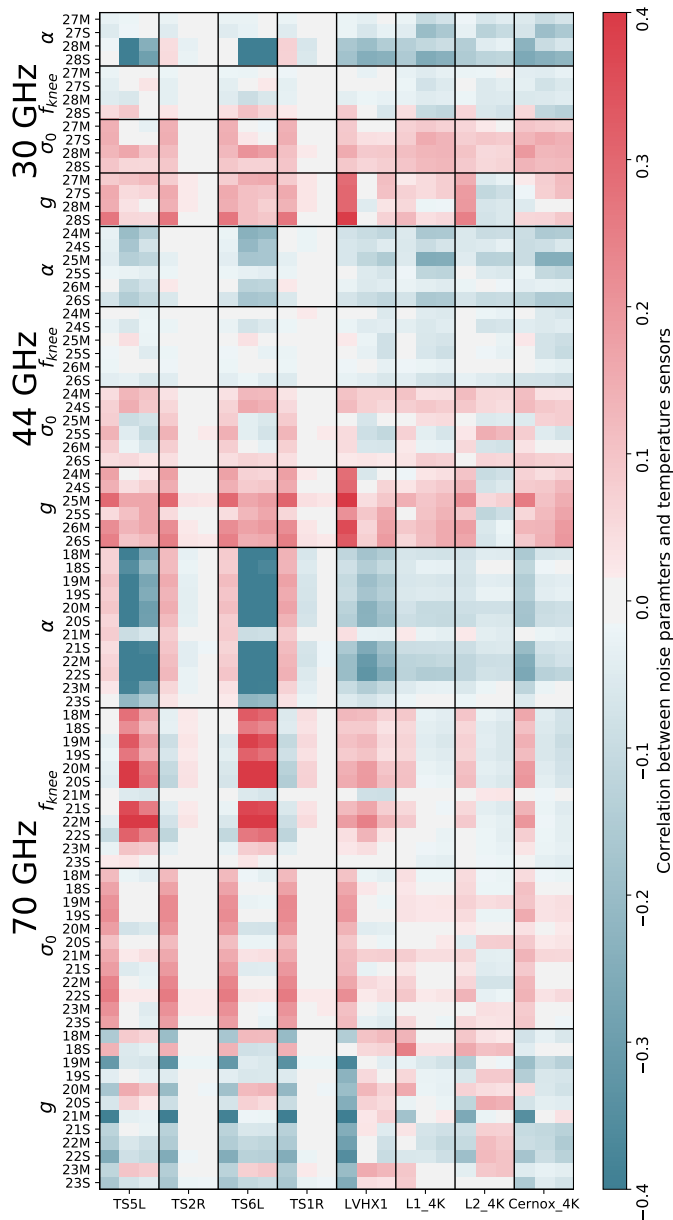
6.5. Correlation with housekeeping data

Next, we correlate the LFI noise parameters with housekeeping data, and in particular with temperature sensor that are relevant for LFI. This is summarized in Fig. 27, showing the correlation coefficients with respect to several sensors that monitor the 20 K stage (TS5L, TS2R, TS6L, TS1R, LVHX1) and the 4 K stage (L1_4K, L2_4K, Cernox_4K). Some significant patterns appear that can be interpreted in terms of the general instrument behavior:

1. For the 70 GHz radiometers, both the rms and the peak-to-peak of the 20 K temperature sensor fluctuations correlate with f_{knee} and anti-correlate with α (i.e., they prefer a steeper power-law slope). This is particularly evident for the TS5L and TS6R sensors, which are located nearby the 70 GHz array. This indicates that the $1/f$ noise of the 70 GHz radiometers is dominated by residual thermal fluctuations in the 20 K stage. A similar trend can be seen also at 30 GHz in the two horn-coupled receivers 28M and 28S. However, the 44 GHz

channels show no sign of this behavior. Combined with the lack of correlation with the 4 K sensors, this is consistent with the hypothesis that the $1/f$ noise of the 44 GHz (and partly the 30 GHz) radiometers is dominated by non-thermal fluctuations.

2. Weaker correlations are seen between the various noise parameters and the 4 K temperature sensors. The lack of significant correlation of the rms and peak-to-peak of 4 K sensors with any of the $1/f$ parameters, f_{knee} and α, is an indication that the 4 K reference loads do not contribute significantly to the radiometers correlated noise.

3. A strong anti-correlation (correlation) of the gain g with the absolute value of the 20 K sensors for the 70 GHz (30–44 GHz) radiometers is observed. Based on the discussion in Sect. 6.3, this pattern can be understood by noting that the 20 K stage temperature systematically increased throughout the mission, driven by sorption cooler adjustments. The same monotonic trend was also on-going in the 300 K stage, which controls the BEM amplifiers. This is thus a spurious
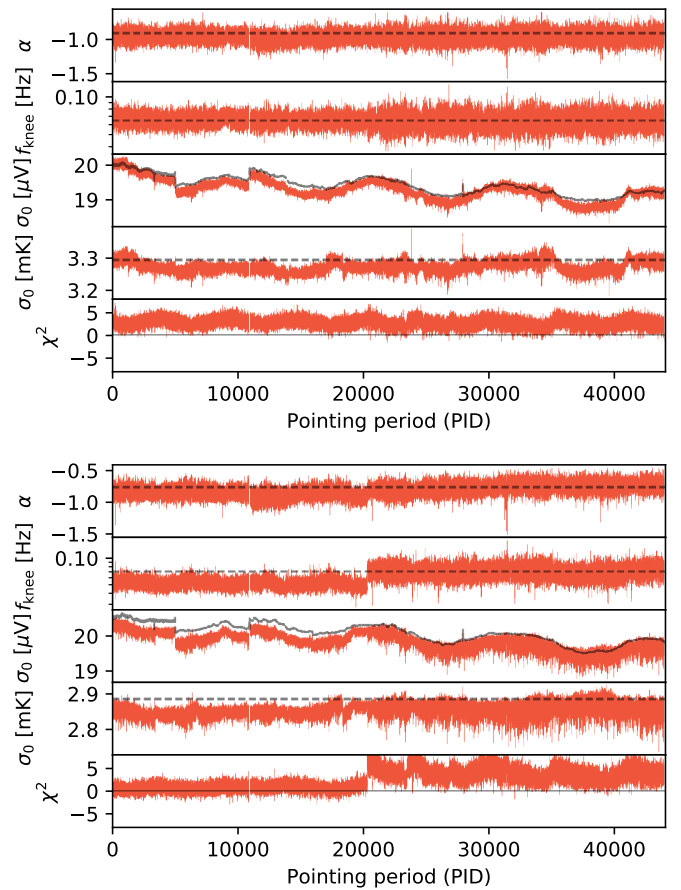
Fig. 28. Evolution of posterior mean noise parameters for radiometers 26M (top) and 26S (bottom). Black curves show corresponding values as derived by, and used in, the official *Planck* LFI DPC pipeline. Note here that the PIDs after about PID 20 000 were not included in the main BEYONDPLANCK run, so the results there are from a much shorter earlier test run, and are hence more noisy.

Fig. 27. Correlation in time, for the complete mission, between noise parameters and the temperature sensors. For each sensor we show the results (from left to right) from the mean temperature, the temperature rms and the peak-to-peak temperature of each sensor within each pointing period. The results here are for the calibrated white noise level, σ_0 [K]. We have imposed a mild highpass-filter in time of the different datasets in order to avoid random correlations on the very longest timescales.
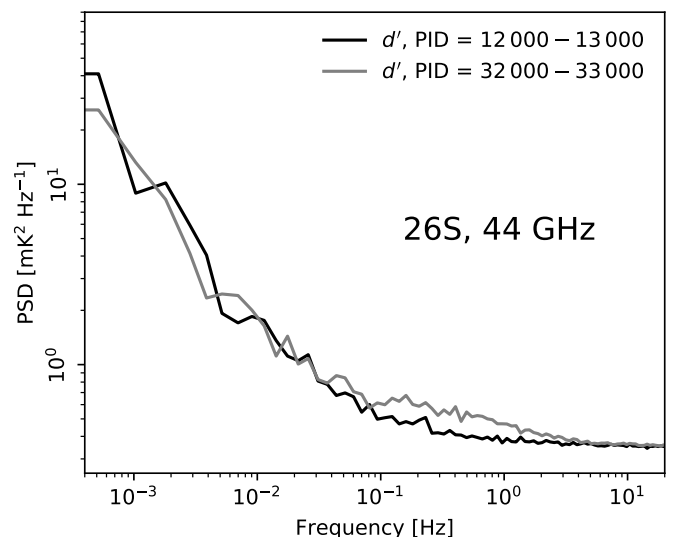
correlation, for which the increasing back-end temperature actually leads to lower (higher) values of g for the 70 GHz (30–44 GHz) radiometers.

6.6. Issues with individual radiometers

In addition to the overall behavior and correlations that are common to many or most radiometers, there are issues that only seem to affect individual radiometers. Here we point out two special cases, namely 26S and 21M.

Fig. 29. PSD of signal subtracted data from radiometer 26S, averaged over 10 PIDs (at intervals of 100 PIDs) in the ranges 12 000–13 000 (black) and 32 000–33 000 (grey). We see that there is significantly more power in the frequency range 10^{-1}–10^1 Hz in the later period.

First, as discussed above, we often find excess noise power in the 30 and 44 GHz channels in the signal-subtracted data at intermediate frequencies, ~0.1–5 Hz. This excess cannot be described with a $1/f$ noise model, and leads to high χ^2 values. The most extreme example of this is the 44 GHz 26S radiometer, as shown in Fig. 28. This figure is identical to the bottom panel Fig. 13, except that masked PIDs are now not omitted. Here we see a jump in f_{knee} around PID 20 800, after which the χ^2 is consistently high with a mean of about 5 σ. This is elucidated in Fig. 29, which compares the noise PSD averaged over 10 PIDs in the 12 000–13 000 range with a corresponding average evaluated in the 32 000–33 000 range. We see an excess in power at intermediate frequencies that is not possible to fit with the $1/f$ noise model. Considering that the *Planck* spin period is 60 s, temporal frequencies of 0.1–1 Hz correspond to angular scales of 6–60° on the sky. This unmodelled noise therefore represents a significant contaminant with respect to large-scale CMB polarization reconstruction, which is one of the main scientific targets for the current BEYONDPLANCK analysis. We therefore choose to exclude all data from 26S after after PID 20 800 (Suur-Uski et al. 2020). To avoid excessive temperature-to-polarization leakage, we also exclude 26M data for the same region. In total, this represents 17 % of the data full 44 GHz data volume, and the BEYONDPLANCK 44 GHz frequency map therefore has a higher white noise level than the corresponding official *Planck* products; but with a more complete noise description.

The sudden degradation of 26S at around PID 21 000 has no simultaneous counterpart in any other LFI radiometer, including the coupled 26M which exhibits a normal behaviour (see Fig. 28). This suggests a singular event within the 26S itself, or in the bias circuits serving its RF components. Since we do not observe significant changes in the radiometer output signal level and no anomalies are seen in the LNAs currents, it is unlikely that the problem resides in the HEMT amplifiers. A more plausible cause would be a degradation of the phase switch performance, possibly due to ageing, instability of the input currents, or loss of internal tuning balance (Mennella et al. 2010; Cuttaia et al. 2009). Indeed sub-optimal operation of the phase switches would not significantly change the signal output level, but is known to introduce excess $1/f$ noise, as verified during the ground testing and in-flight commissioning phase.

The second anomalous case is the 70 GHz 21M radiometer. While the noise properties of the other 70 GHz channels are internally significantly correlated, this particular channel does not show similar correlations. The reason for the different behavior of 21M is still not fully understood. However, as shown for PID 2201 in Fig. 30, this particular radiometer exhibits a typical "popcorn" or "random telegraph" noise, i.e., a white noise jumping between two different offset states. During ground testing this behavior was noted in the undifferenced data of LFI21 and LFI23 and ascribed to bimodal instability in the detector diodes. The effect was then recognized in-flight and this prevented proper correction of ADC nonlinearity effect (Planck Collaboration III 2014). However, because the timescale of diode jumps between states (typically a few minutes) is longer than the differencing between sky and reference load (0.25 ms, corresponding to the phase switch frequency of 4 kHz), the effect is efficiently removed in the differenced data. In the current analysis, we actually observe popcorn behavior in the differenced data, suggesting either an increased instability of the affected diode in 21M (possibly due to aging), or a different origin of the effect. Popcorn noise has been also found in some HFI channels (Planck HFI Core Team 2011). We have not seen any sign of popcorn noise in any of the other LFI channels besides 21M,
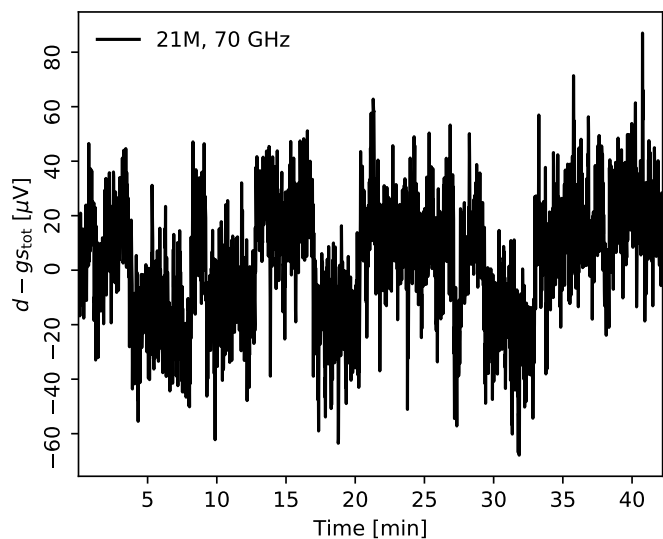
Fig. 30. Signal subtracted data from radiometer 21M for PID 2201. The data are averaged over a one second timescale.

but we have also not performed a deep dedicated search for it. However, the fact that the χ^2 distribution for channel 21M appears acceptable suggests that this effect, even if surviving in the differenced data stream, happens at a sufficiently long timescale that $\boldsymbol{n}_{\text{corr}}$ is able to absorb it, preventing it from leaking into other astrophysical components.

7. Conclusions

This paper has two main goals. First, it aims to describe Bayesian noise estimation within a global CMB analysis framework (BeyondPlanck Collaboration 2020). As such, this work represents the first real-world application and demonstration of methods originally introduced by Wehus et al. (2012), while at the same time taking advantage of important numerical improvements introduced by Keihänen et al. (2020). The second main goal is to apply this method to the *Planck* LFI measurements to characterize their noise properties at a more fine-grained level than done previously (Planck Collaboration II 2020).

An important question regarding the original work of Wehus et al. (2012) was whether the method would be practical for real-world observations, or whether it was too computationally expensive to be useful in a real pipeline. We are now in a position to conclusively answer this question: As summarized by (BeyondPlanck Collaboration 2020; Galloway et al. 2020a), the noise estimation step in the BEYONDPLANCK pipeline accounts for 38 % of the total runtime, or 48 CPU-hours per sample for the 70 GHz channel, most of which is spent Fourier transforming the raw time-ordered data. As such, exact Bayesian noise estimation certainly is an expensive pipeline component—but it is by no means not prohibitive. Additionally, it is important to note that Bayesian correlated noise sampling replaces both traditional mapmaking and noise covariance matrix evaluations (Keihänen et al. 2020; Suur-Uski et al. 2020), which are two of the most expensive procedures in a traditional CMB analysis pipeline (Planck Collaboration I 2020), and, in fact, this leads to lower computational requirements overall. As an example, we note that a full BEYONDPLANCK Gibbs sample (which includes both low- and high-level processing with all LFI channels) costs 163 CPU-hours, while producing a single component of the full

Planck Full Focal Plane (FFP) simulation of the 70 GHz channel costs 9360 CPU-hours. Likewise, we also note that the current BEYONDPLANCK analysis was run on an in-house cluster with 416 cores and 9 TB of RAM, while the *Planck* simulations were produced on a large national computing center with $O(10^5)$ cores (Planck Collaboration I 2020; Planck Collaboration Int. LVII 2020). We believe that the computational speed of this method alone should make it an attractive option for other CMB experiments, not to mention the possibilities of performing joint exact Bayesian analysis.

As far as LFI-specific results are concerned, the current results point toward generally complex noise behaviour with subtle contributions from origins that have not yet been fully accounted for. Most notably, the noise properties of each LFI radiometer vary significantly in time, and depend sensitively on the thermal environment of the instrument. For the 70 GHz channel, for which the correlated noise amplitude (and knee frequency) is generally low, most of these variations may be described in terms of a simple $1/f$ model with time-dependent parameters. With very few exceptions, the time-domain χ^2 of this channel is statistically acceptable throughout the mission.

However, for the 30 and 44 GHz channels a more complex picture has emerged. For these, the χ^2 is generally high by 2–3 σ per PID, and with significant variations as a function of time. Multiple observations suggest a yet undetected source of non-thermal correlated noise in the 44 GHz (and at a lower level in the 30 GHz radiometers) that is responsible for mild, and possibly time-varying, deviations from the simple $1/f$ model. Inspection of individual PIDs indicates the presence of excess power between 0.1 and 5 Hz, well above the *Planck* scanning frequency of 0.017 Hz, thereby affecting the angular scales that are relevant for large-scale CMB polarization science. Our analysis suggests that these effects are not due to temperature fluctuations, but rather associated with other effects, such as electrical instabilities or other environmental issues. We have carried out a preliminary investigation by correlating the LFI radiometers whose LNA bias were supplied by common electronics groups,[6] but we have found no compelling evidence of correlations or anomalies. Many other electrical effects must be studied by exploiting all the available housekeeping information. Most of the spikes in the rms of the temperature sensors (see, e.g., Fig. 20) are readily understood as due to commanded cooler adjustments, but a few of them deserve further investigation. The influence of transient perturbations should also be systematically investigated, including the possible effect of cosmic rays and solar flares.

A complete and quantitative analysis will require a detailed thermal model of the full instrument that includes the back-end unit and interfaces with the V-grooves, coupled with thermal susceptibility parameters of the relevant components (LNAs, OMTs, waveguides, BEMs, detector diodes, data acquisition electronics). Such a detailed study is beyond the scope of this work, but this is now made possible through the present study, and it will become a primary target for future BEYONDPLANCK LFI analysis.

A separate issue appears to be associated with the gain model, which for some radiometers exhibits larger temporal variations than might be expected from housekeeping data. This might be connected with a number of strong stripes in the 44 GHz correlated noise map, which affects large fractions of the sky at the $1\,\mu$K level, which are highly relevant for large-scale CMB polarization reconstruction. Of course, problems with the 44 GHz channel have been reported by the *Planck* team ever since the first data release (Planck Collaboration VI 2014; Tauber et al. 2019; Planck Collaboration II 2020), and it was therefore omitted from the main *Planck* CMB polarization analysis (Planck Collaboration IV 2020). The current method and results do not yet resolve these problems, but hopefully they shine new light on the issue that might help resolve it through further modelling. In particular, understanding and mitigating the χ^2 excesses at 30 and 44 GHz (possibly by generalizing the $1/f$ noise model) and the stripes at 44 GHz (possibly through more robust gain modelling) should be a top priority for future BEYONDPLANCK analyses.

In general, the detailed BEYONDPLANCK modelling approach allows us to highlight a number of subtle systematic patterns in the LFI radiometers that were already noted and reported in previous analyses, but only now, for the first time, have been possible to elucidate and understand in greater detail. Examples are a detailed characterization of the nature of seasonal modulations and long term drifts, and correlations between instrument noise parameters with temperature sensor read-out information. These methods are likely to play a central role in the analysis of future high-sensitivity CMB *B*-mode experiments, for instance *LiteBIRD* (Sugai et al. 2020).

---

[6] There were four such power groups in LFI, feeding the radiometers associated with the following horn sets: (19-20-28), (18-26), (21-22-24-27), (23-25).

References

Abazajian, K., Addison, G., Adshead, P., et al. 2019, arXiv e-prints, arXiv:1907.04473
Ade, P., Aguirre, J., Ahmed, Z., et al. 2019, J. Cosmology Astropart. Phys., 2019, 056
Andersen et al. 2020, A&A, in preparation [arXiv:201x.xxxxx]
Ashdown, M. A. J., Baccigalupi, C., Balbi, A., et al. 2007, A&A, 471, 361
Bennett, C. L., Larson, D., Weiland, J. L., et al. 2013, ApJS, 208, 20
Bersanelli, M., Mandolesi, N., Butler, R. C., et al. 2010, A&A, 520, A4
BeyondPlanck Collaboration. 2020, A&A, in preparation [arXiv:201x.xxxxx]
Bond, J. R., Jaffe, A. H., & Knox, L. 2000, ApJ, 533, 19
Colombo et al. 2020, A&A, in preparation [arXiv:201x.xxxxx]
Cuttaia, F., Mennella, A., Stringhetti, L., et al. 2009, Journal of Instrumentation, 4, 2013
Cuttaia, F. & Terenzi, L. 2011, Planck-LFI Technical Note, 098
Galloway et al. 2020a, A&A, in preparation [arXiv:201x.xxxxx]
Galloway et al. 2020b, A&A, in preparation [arXiv:201x.xxxxx]
Gjerløw et al. 2020, A&A, in preparation [arXiv:201x.xxxxx]
Gorski, K. M. 1994, ApJ, 430, L85
Hanany, S., Alvarez, M., Artis, E., et al. 2019, arXiv e-prints, arXiv:1902.10541
Hivon, E., Górski, K. M., Netterfield, C. B., et al. 2002, ApJ, 567, 2
Keihänen et al. 2020, A&A, in preparation [arXiv:201x.xxxxx]
Lamarre, J., Puget, J., Ade, P. A. R., et al. 2010, A&A, 520, A9
Lewis, A. & Bridle, S. 2002, Phys. Rev. D, 66, 103511
Mennella, A., Bersanelli, M., Butler, R. C., et al. 2010, A&A, 520, A5
Page, L., Hinshaw, G., Komatsu, E., et al. 2007, ApJS, 170, 335
Paradiso et al. 2020, A&A, in preparation [arXiv:201x.xxxxx]
Planck HFI Core Team. 2011, A&A, 536, A4
Planck Collaboration I. 2011, A&A, 536, A1
Planck Collaboration II. 2011, A&A, 536, A2
Planck Collaboration I. 2014, A&A, 571, A1
Planck Collaboration II. 2014, A&A, 571, A2
Planck Collaboration III. 2014, A&A, 571, A3

Planck Collaboration VI. 2014, A&A, 571, A6
Planck Collaboration II. 2016, A&A, 594, A2
Planck Collaboration XII. 2016, A&A, 594, A12
Planck Collaboration I. 2020, A&A, 641, A1
Planck Collaboration II. 2020, A&A, 641, A2
Planck Collaboration III. 2020, A&A, 641, A3
Planck Collaboration IV. 2020, A&A, 641, A4
Planck Collaboration V. 2020, A&A, 641, A5
Planck Collaboration VI. 2020, A&A, 641, A6
Planck Collaboration Int. LVII. 2020, A&A, in press [arXiv:2007.04997]
QUIET Collaboration, Bischoff, C., Brizius, A., et al. 2011, ApJ, 741, 111
Sugai, H., Ade, P. A. R., Akiba, Y., et al. 2020, Journal of Low Temperature Physics, 199, 1107
Suur-Uski et al. 2020, A&A, in preparation [arXiv:201x.xxxxx]
Suzuki, A., Ade, P. A. R., Akiba, Y., et al. 2018, Journal of Low Temperature Physics, 193, 1048
Svalheim et al. 2020a, A&A, in preparation [arXiv:201x.xxxxx]
Svalheim et al. 2020b, A&A, in preparation [arXiv:201x.xxxxx]
Tauber, J. A., Nielsen, P. H., Martín-Polegre, A., et al. 2019, A&A, 622, A55
Tegmark, M. 1997, ApJ, 480, L87
Tegmark, M., Taylor, A. N., & Heavens, A. F. 1997, ApJ, 480, 22
Terenzi, L., Salmon, M. J., Colin, A., et al. 2009, Journal of Instrumentation, 4, 2012
Villa, F., Terenzi, L., Sandri, M., et al. 2010, A&A, 520, A6
Wandelt, B. D., Larson, D. L., & Lakshminarayanan, A. 2004, Phys. Rev. D, 70, 083511
Wehus, I. K., Næss, S. K., & Eriksen, H. K. 2012, ApJS, 199, 15